

# THERMOGRAPHIC PHOSPHOR MEASUREMENTS OF SHOCK-SHOCK INTERACTIONS ON A SWEEP CYLINDER

Michelle L. Jones, Scott A. Berry  
NASA Langley Research Center, Hampton, VA, 23681

The effects of fin leading-edge radius and sweep angle on peak heating rates due to shock-shock interactions were investigated in the NASA Langley Research Center 20-inch Mach 6 Air Tunnel. The cylindrical leading-edge fin models, with a radius varied from 0.25 to 0.75 inches, represent wings or struts on hypersonic vehicles. A 9° wedge generated a planar oblique shock at 16.7° to the flow that intersected the fin bow shock, producing a shock-shock interaction that impinged on the fin leading edge. The fin sweep angle was varied from 0° (normal to the free-stream) to 15° and 25° swept forward. These cases were chosen to explore three of six characterized shock-shock interaction types. Global temperature data were obtained from the surface of the fused silica fins using phosphor thermography. Metal oil flow models with the same geometries as the fused silica models were used to visualize the streamline patterns for each angle of attack. High-speed zoom-schlieren videos were recorded to show the features and any temporal unsteadiness of the shock-shock interactions. The temperature data were analyzed using one-dimensional semi-infinite as well as one- and two-dimensional finite-volume methods. These results were compared to determine the proper heat transfer analysis approach to minimize errors from lateral heat conduction due to the presence of strong surface temperature gradients induced by the shock interactions. The general trends in the leading-edge heat transfer behavior were similar for each explored shock-shock interaction type regardless of the leading-edge radius. However, the dimensional peak heat transfer coefficient augmentation increased with decreasing leading-edge radius. The dimensional peak heat transfer output from the two-dimensional code was about 20% higher than the value from a standard, semi-infinite one-dimensional method.

## Variables

$c_h$  = convective heat transfer coefficient (kg/m<sup>2</sup>-s)  
 $h$  = enthalpy (kJ/kg)  
 $M$  = Mach number  
 $P$  = pressure (psi or psia)  
 $\dot{q}$  = rate of heat transfer (W)  
 $r$  = radial direction in cylindrical coordinates  
 $Re$  = Reynolds number  
 $t$  = time (s)  
 $T$  = temperature (°F or K)  
 $U$  = velocity (ft/s)  
 $V$  = volume (m<sup>3</sup>)  
 $x$  = distance into test article from surface (m)  
 $z$  = lateral direction in cylindrical coordinates  
 $\varepsilon$  = emissivity of phosphor-coated fused silica models  
 $\sigma$  = Stefan-Boltzmann constant (W/m<sup>2</sup>-K<sup>4</sup>)  
 $\rho$  = density (slug/ft<sup>3</sup>)

## Subscripts

aw = adiabatic wall  
w = wall (surface of test article)  
FR = Fay-Riddell  
ref = reference from mean baseline heating  
t,1 = reservoir stagnation  
tw = tunnel wall  
 $\infty$  = free-stream conditions

## Acronyms

AoA = angle of attack  
BL = boundary layer  
BS = bow shock  
CAD = Computer-Aided Design  
CFD = Computational Fluid Dynamics  
CMM = Coordinate Measuring Machine  
IHEAT = Imaging for Hypersonic Experimental Aeroheating Testing  
IS = incident shock  
LAL = Langley Aerothermodynamics Laboratory  
LaRC = Langley Research Center  
NASA = National Aeronautics and Space Administration  
NASP = National Aero-Space Plane  
RS = reflected shock  
RTF = Shuttle Return to Flight program  
RTV = Room-Temperature Vulcanized silicone rubber  
Scramjet = Supersonic combustion ramjet  
SG = shock generator  
SL = shear layer  
TP = triple point  
TPS = Thermal Protection System  
UV = ultra-violet (radiation)

## 1. Introduction

Commercial, government and military applications rely on research into safe, reliable hypersonic technology. Vehicles designed to fly at hypersonic speeds, such as the now retired Space Shuttle Orbiter and planes with integrated ramjet or supersonic combustion ramjet (scramjet) engines, can be subjected to a phenomenon called

shock-shock interactions that cause significant, localized surface temperature and pressure augmentations [1]. Interactions between the vehicle bow shock and the shock around a strut or a wing leading edge can compromise the vehicle's structural components in the absence of protective measures. Numerous experiments have investigated shock interaction behavior and heating effects that occur in the hypersonic flight regime to aid in the development of sufficient Thermal Protection Systems (TPS). These studies helped classify shock interaction types and pointed to the need for improved spatial resolution of the data in the regions affected by the interactions, as well as the potential need for two-dimensional (2D) heat transfer analyses in addition to the standard one-dimensional techniques if a strong lateral temperature gradient exists. Measurement techniques have gradually improved to provide better spatial resolution in shock-interaction heat transfer analyses.

Shock-shock interactions in hypersonic flow, as described in this study, involve an oblique incident shock generated by a flat plate shock generator (SG) that intersects a bow shock around a blunt body. Edney [1] identified six types of interactions between bow shocks around blunt bodies and incident shocks. The relative angle between the incident shock and the bow shock, as well as the strengths of these two shocks, dictate the features of the resulting shock impingement, such as the angle of the reflected shock, the number of shear layers that form, or the presence of a supersonic jet. These shock-shock interactions are sketched in Figure 1. Of the six types, the Type III and IV interactions are likely to produce the worst heating to the vehicle since the shear layer or jet impinges directly on the surface. Since the time of Edney's study, one additional sub-type has been added to the shock-shock interaction lexicon, the Type IVa, in which the supersonic jet largely misses the surface of the body.

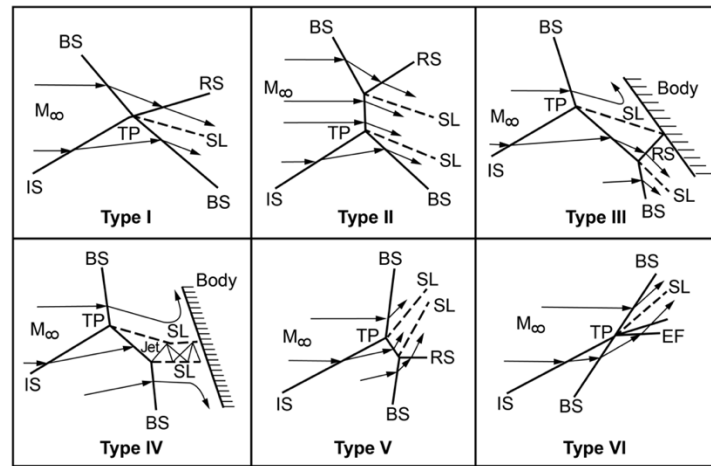


**Figure 1. Edney catalogued six shock interaction types, IS = incident shock, BS = bow shock, RS = reflected shock, EF = expansion fan, TP = triple point, SL = shear layer.**

In the current study, Type III and Type IV (both direct and glancing) shock-shock interactions were investigated. Edney [1] states that the peak heating associated with a Type III interference is attributed to a free shear layer attaching to the body, much like in separated flows. The flow between the bow shock and the shear layer is supersonic in this type of an interaction for a blunt body. The Type IV interaction yielded the highest peak heating augmentation in Edney's study. In this interaction, a supersonic jet either curls upward (as in a Type IVa interaction) or impinges directly on the blunt body as in Figure 1. Reflected shocks between two shear layers in this supersonic jet produce shock triangles that are referred to as a "shock train."

The necessity of considering heating augmentation due to shock-shock interactions is evident in real flight scenarios. Strong Type III and IV shock-shock interactions can exist during hypersonic flight on forward swept leading edges inside scramjet engines [2]. Potential applications for scramjet vehicles include cruise missiles, long-range aircraft, and single-stage-to-orbit (SSTO) space vehicles [3]. Notable scramjet projects include the X-43A, described in [4] and [5], the X-51A [6], and the National Aero-Space Plane (NASP) concept vehicle, also known as the X-30 [3]. The Hypersonic International Flight Research Experimentation (HIFiRE) Program is still investigating scramjet propulsion with wind tunnel and flight experiments [7]. The heating augmentation due to shock-shock interactions affects scramjet development since engine or structural failure is unacceptable in either hypersonic missiles used to quickly strike long-range targets or in manned hypersonic vehicles.

Edney [1] describes three general cases in which shock-shock interactions could occur in flight. During the flight of a missile, the bow shock that originates at the nose of the missile can interact with the shock around an attached fuel tank or a booster. Secondly, a 2D "shock-on-cowl" interaction involves a planar extraneous shock and

the shock around a cowl lip on a vehicle with a ramjet or a scramjet engine. Numerous shock-shock interaction studies focused on the 2D shock-on-cowl interaction in which a planar incident shock intersects the bow shock around a cowl leading edge that is parallel to the plane of the incident shock (as in [8], [9], [10], [11]). The current test set-up simulates the third type of interaction, a 3D “shock-on-fin” interaction due to an intersection between a bow shock around an aircraft fuselage and the shock around a strut (fin) leading edge. The last two types of interactions on a hypersonic vehicle are shown for reference in Figure 2.

### SHOCK/SHOCK INTERFERENCE ON ENGINE LEADING EDGES

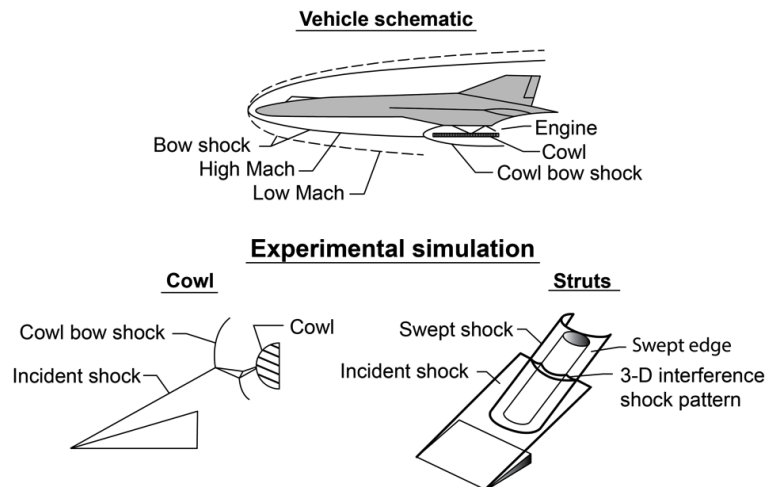


**Figure 2. Hypersonic flight vehicle configuration.**

The X-15-2 research plane flew in a few test flights with a dummy ramjet attached to the fuselage using a pylon [12]. During one flight, the X-15-2 plane reached a record speed of Mach 6.7, producing a shock-shock interaction that impinged on the pylon and caused such severe heating damage to the pylon and the X-15-2 fuselage (see Figure 3) that the dummy engine separated from the vehicle when the plane slowed down to about Mach 1. Watts recommends caution when designing hypersonic vehicles exposed to shock-interference heating, since shock impingement could raise vehicle temperatures beyond the maximum allowable temperatures of “high-performance metals” unless the structural geometry is “designed to minimize aerodynamic heating”.



**Figure 3. Damaged X-15-2 pylon from Mach 6.7 shock interference heating.**

The Columbia accident highlights the potential for shock-interaction damage on a hypersonic vehicle if the designed TPS is compromised [13]. A piece of insulation foam dislodged from the solid rocket boosters during the launch and struck a reinforced carbon/carbon panel on the Shuttle’s left wing leading edge [14] in a region that would eventually be exposed to strong shock-shock interactions during re-entry into the Earth’s atmosphere [13]. The general conclusion is that heated air was ingested into a small breach in the leading edge of the Shuttle’s left wing, yielding elevated temperatures, burning through instrumentation wiring, and finally causing the structural failure of Columbia.

Berry and Nowak [15] experimentally investigated the effect of fin sweep angle on the expected increase in the peak heating on a leading edge or strut of a hypersonic vehicle, perhaps within a scramjet engine as in the proposed

NASP, due to different types of 3D shock-shock interactions. Temperatures measured using Macor® test articles instrumented with thin-film gages were reduced using a 1D heat transfer code. Berry and Nowak postulate that the non-dimensional peak heating increase for a Type IV interaction in a wind tunnel run with a 0.25 in-radius test article at a  $-15^\circ$  angle of attack (AoA) might grow from nearly seven times the baseline value to a factor of ten if lateral conduction effects were considered in the heat transfer analysis. The peak heating increase for a run with the test article at a  $-25^\circ$  AoA (a Type III interaction) was again nearly seven times the baseline value. Most of the wind tunnel runs in [15] were conducted at a Reynolds (Re) number of  $2.1 \times 10^6/\text{ft}$  with the flat plate SG at  $9^\circ$  to the flow.

Bushnell conducted an experiment in the Langley Mach 8 variable-density wind tunnel that involved an incident shock from a  $12^\circ$  wedge impinging on the bow shock around 1.0 in-diameter cylinders [16]. These stainless steel cylinders were swept forward either  $45^\circ$  or  $60^\circ$ , yielding Type VI shock-shock interactions. Two cylinders were instrumented with thermocouples with a minimum spacing of 0.25 in between the sensors. Bushnell calculated the heat transfer along the leading edge from the thermocouple temperature data. Bushnell concludes that the intersection between the incident shock and bow shock did not produce a peak in the heat transfer. However, the smallest separation of the sensors on these models is nearly 17 times larger than the 0.015 in minimum thin-film-gage spacing in [15], which suggests a peak in heat transfer could have existed in that region without being detected.

Additional experiments have investigated shock-shock interactions on transverse cylinders using discrete gages along the leading edge, such as the studies by Keyes and Hains [17] and Hiers and Loubsky [18]. Carter and Carr [19] performed a flight experiment to study the heat transfer to a 0.75 in-diameter unswept cylinder attached to a rocket in a 3D shock-on-fin interaction. Temperature data was obtained remotely from thermocouples on the cylinder when the two-stage rocket launched from the National Aeronautics and Space Administration (NASA) Wallops Island and accelerated up to Mach 5.5.

Walker and Scott [20] (and Walker [21]) used the thin-film-gage data from reference [15] as inputs to 1D and 2D inverse conduction codes for sample cases with the Macor® and Upilex® test articles to estimate the heat flux due to a shock-shock interaction. Walker and Scott neglect the effects of curvature of the models in both codes, assuming the geometry behaves as a flat plate. The 2D code results for the Macor® test articles in [20] reveal a difference of  $\pm 20\%$  at the heat flux peaks and valleys compared to the results from a 1D code with the same temperature inputs. The heat flux values outside of the peak are very similar between the two methods. Walker and Scott conclude that the heat flux calculations could be improved by increasing the spatial resolution of the acquired temperature data.

Daryabeigi et al. [22] analyzed experimental infrared temperature data from the LaRC 20-Inch Mach 6 Air Tunnel using finite-volume (FV) codes that implemented the Crank Nicholson method (1D) or the ADI algorithm (2D and 3D) to approximate the conduction in a Macor® model of the Hyper-X fore body. The heating striations produced by streams of injected gas were analyzed with codes that either neglected or included lateral conduction in the model. Daryabeigi et al. found the 1D, through-thickness heat transfer approximation yielded errors of up to  $\pm 20\%$  compared to results from a 2D FV code.

The results of the current study contribute to the knowledge of 3D shock-on-strut interactions in hypersonic flight. This research is the first known published study in which global thermal imaging techniques are used in conjunction with multi-dimensional thermal analyses to investigate high heating rates associated with shock-shock interactions. The phosphor thermography technique provided temperature and heat transfer data with an increased spatial resolution compared to the discrete sensors typically used in prior shock-shock interaction studies. Additionally, the current study provides information about shock-shock interactions from improved experimental tools such as high-speed zoom schlieren and two separate oil-flow techniques.

## 2. Facility

The facility used for the present study was the 20-Inch Mach 6 Air Tunnel, a tunnel in the Langley Aerothermodynamics Laboratory (LAL) at NASA Langley Research Center (LaRC) [23]. This perfect gas facility has well-characterized flow uniformity and composition [24]. The tunnel reservoir stagnation pressure and temperature,  $P_{t,1}$  and  $T_{t,1}$ , are accurate to within  $\pm 2\%$ . The LaRC 20-Inch Mach 6 Air Tunnel is a blow-down wind tunnel. Dry air from two high-pressure bottle fields is transferred to a 600-psia reservoir, where an electrical resistance heater heats the air to a maximum temperature of  $1000^\circ\text{R}$ . The flow passes through two filters installed between the heater and the settling chamber before entering the test section at Mach 6, as shown in Figure 4. The upstream filter captures particles larger than  $10\text{ }\mu\text{m}$ , and the downstream filter is rated to block  $5\text{-}\mu\text{m}$  particles. The maximum tunnel operating pressure is 475 psia [25].

The settling chamber contains a perforated conical baffle at the entrance and internal screens. The top and bottom walls of the fixed-geometry, two-dimensional nozzle are contoured and the side walls are parallel. The 0.34 in by 20 in nozzle throat opens into a 20.5 in by 20 in test section. The nozzle length from the throat to the test section window

center is 7.45 ft. This wind tunnel exhausts either into combined 41-ft-diameter and 60-ft-diameter vacuum spheres, a 100-ft-diameter vacuum sphere, or to the atmosphere through an annular steam ejector. Free-stream flows with Mach numbers between 5.8 and 6.1 and Re numbers between  $0.5 \times 10^6/\text{ft}$  and  $7.3 \times 10^6/\text{ft}$  are possible in this facility [26]. Runs at the lower flow Re numbers ( $0.5 \times 10^6/\text{ft}$  to  $2.0 \times 10^6/\text{ft}$ ) are easier to set up and to conduct when the air is exhausted to the steam ejector.

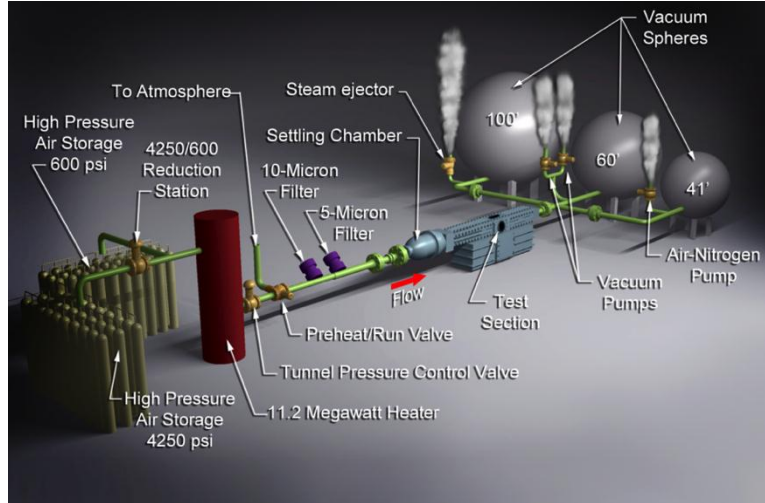


**Figure 4. LAL 20-Inch Mach 6 Air Tunnel.**

Test articles are typically mounted on the arc-sector injection system located in a housing below the test section. This injection system is used to quickly insert the model into the flow after the tunnel has been started. Aeroheating tests generally have total run times of 30 sec, with typical model injection times of approximately 1.5 sec and a model residence time on the tunnel centerline of approximately 5-10 sec. The actual mean flow conditions for this study are provided in Table 1. These flow conditions were calculated by averaging the parameters for thirty runs at  $Re = 2.1 \times 10^6/\text{ft}$  and two runs at  $Re = 1.1 \times 10^6/\text{ft}$ . The parameters for a  $Re = 4.1 \times 10^6/\text{ft}$  correspond to the one run that was conducted at that Re number.

**Table 1. Actual mean flow conditions in Tests 6976 and 6983 in 20-Inch Mach 6 Air Tunnel.**

$M_\infty$	$Re_\infty, \text{ft}^{-1} \times 10^{-6}$	$P_{t,1}, \text{psia}$	$T_{t,1}, ^\circ\text{R}$	$\rho_\infty, 10^{-4} \text{slug}/\text{ft}^3$	$T_\infty, ^\circ\text{R}$	$U_\infty, \text{ft}/\text{s}$
5.90	1.1	60.5	875.1	0.33	110.3	3035
5.96	2.1	125.5	898.5	0.63	111.3	3082
6.00	4.1	252.2	901.6	1.23	110.5	3087

### 3. Experimental set up

The key components shown in Figure 5 are the SG, a flat plate with a sharp leading edge that is inclined at  $9^\circ$  from horizontal to produce a  $16.7^\circ$  planar incident shock at Mach 6, and the test article, inclined at  $15^\circ$  in the figure. Figures 5 and 6 show graphical representations of the test hardware utilized for this study. Similar images of these computer-aided design (CAD) models were used prior to the experiment to ensure the visibility of the leading edge through the top and side wind tunnel windows for each run with the upper tip of the test article swept  $0^\circ$ ,  $15^\circ$ , or  $25^\circ$  forward of vertical, defined as  $0^\circ$ ,  $-15^\circ$ , and  $-25^\circ$  test article angles of attack (AoA), respectively.

Figure 5 also shows the arc sector positioned below the test section in the 20-Inch Mach 6 Air Tunnel. Ten bolts (five on each side) secure an I-beam to the arc sector using a 1 in-thick spacer to center the test article in the core flow of the wind tunnel. Three bolts on either side secure the strut to the I-beam. The strut head plate is bolted to the top surface of the strut to support a flat plate SG angled  $9^\circ$  from horizontal. The stainless steel SG is 6 in wide and 17 in long. A stainless steel support that allows height adjustments is bolted into the strut head plate behind the SG. This supports holds the test article above the SG using a 0.5 in-diameter sting. The appropriate test article is bolted to the sting through a component used to change the angle of attack of the test article, called the “fin adjuster”.

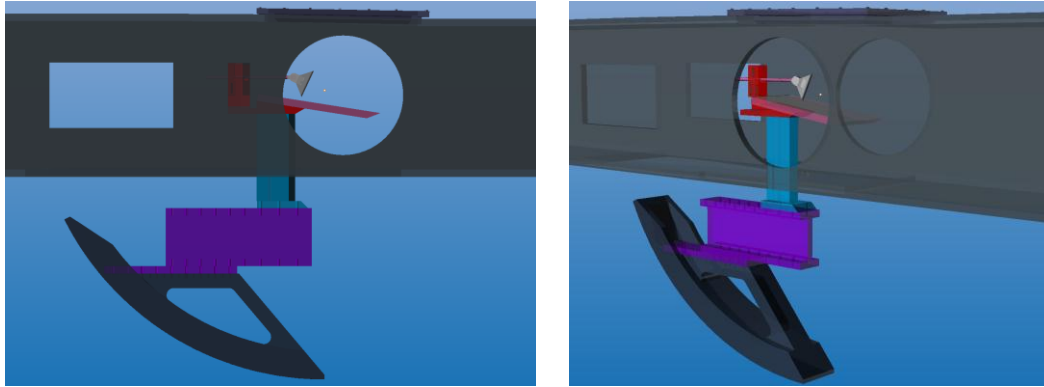


**Figure 5. Side-view renderings of tunnel set-up with arc sector, I-beam, and strut.**

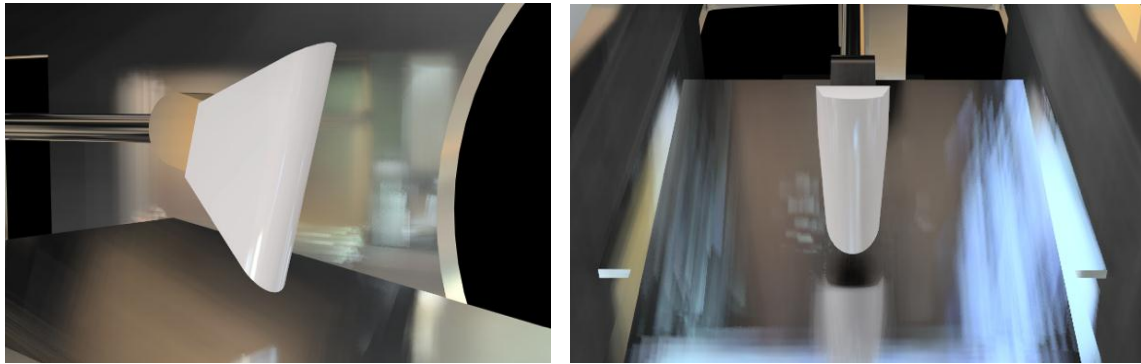


**Figure 6. Side- and top-view renderings of 0.5 in-radius fused silica test article at  $-15^\circ$  AoA.**

In Figure 7, the test article support system is retracted into the “box” below the tunnel test section. A single embedded thermocouple is installed at the surface of the fused silica test articles. The thermocouple is just below the phosphor coating and the bead location is labeled in the figure. The stainless steel fin adjuster is also shown more clearly in the inset image. The adjuster is secured to the sting on one side using a 10-32 bolt, nut and washer and bolted on the other side to a metal insert with threaded holes that is bonded into the fused silica test article. A hinge pin with a retaining ring allows the test article to be rotated through any angle of attack between  $-45^\circ$  and  $45^\circ$  from horizontal. An inclinometer was used to set the angle of attack before the bolt on the fin adjuster was tightened.

The test article was always positioned at least 0.5 in above the flat plate SG or the strut head plate to eliminate interactions between the tip of the test article and the flat plate boundary layer (BL) flow. During some of the runs in which the 0.75 in-radius test articles were angled at  $-25^\circ$ , the test article was raised to 0.75 in above the SG plate. Otherwise, the larger bow shock around this test article intersects the flat BL plate far enough ahead of the test article to produce additional interactions that impinge on the surface of the test article. Flow density gradients behind the test articles and shock-BL interactions with the flow over the SG are discussed more in [27].

Oil-flow tests were conducted to visualize surface streamlines in the vicinity of the off-surface shock-shock interactions to provide insight into the flow behavior. Metal test articles cut from 15-5 stainless steel in a wire electrical discharge machine were used instead of ceramic test articles to minimize the likelihood that the model surface would absorb the oil during a run, thus, allowing the test articles to be reused. The surfaces of these test articles were polished smooth and covered with multiple layers of Rust-Oleum® high-temperature BBQ flat black paint (heat resistant up to 1200 °F) to provide sufficient contrast with a white-pigmented oil in videos and images during and after the oil-flow wind tunnel runs.

The fused silica (heat transfer) test article fabrication process began by generating CAD models from drawings of the legacy test articles in [15] with slightly modified dimensions to achieve a  $7^\circ$  angle on either side of the leading half cylinder. The CAD geometries were used to generate wax patterns and then molds of the test articles. Fused silica was poured into the molds using a pour gate (an access hole) built into the model geometry. Due to the small gate size for the test article geometries in this study, the mold was filled with fused silica and no attempt was made to pour out the excess material as in the typical “pour-and-dump” technique. This modified process created solid, porous test articles and facilitated a two-dimensional conduction assumption through a half cylinder to represent the test article leading edge in the FV heat transfer codes.



The cast fused silica test article geometries include an opening in the back to accommodate a mounting plate, which is a metal insert with drilled and tapped holes for screws to attach the model to the sting and the support hardware. The opening includes a 0.005 in clearance on four sides of the model to permit the application of a high-temperature silicone to bond the metal inserts into the sintered test articles. One small, custom-built thermocouple was installed in each of the primary fused silica test articles. These thermocouples measured the change in temperatures between the time the pre-run phosphor thermography image was recorded and the time the run began to offset the leading-edge, pre-run temperatures input to the 1D and 2D FV codes in the heat transfer analyses. Finally, the fused silica test articles were covered with a phosphor mixture composed of ZnCdS: Ag, Ni and  $\text{La}_2\text{O}_2\text{S:Eu}^{3+}$ . These components work together as a two-color relative intensity phosphor coating that is sensitive to temperature changes on the surface of a wind tunnel model.

Fiducial marks are dots applied to a test article in specified locations that are used to correlate distances between features in an image to the physical dimensions of the test article. Fiducial marks were applied to the oil-flow and the phosphor-coated test articles in the same pattern for all the test articles that share the same nose radius. The Quality Assurance Branch at NASA Langley applied fiducial marks to the surface of the fused silica test articles using Dykem® Hi-Spot blue ink [28] and the oil-flow test articles using orange Testors® fluorescent enamel paint. The orange paint provided a sharp contrast between the black surface paint and the white oil pigment during the oil-flow runs.

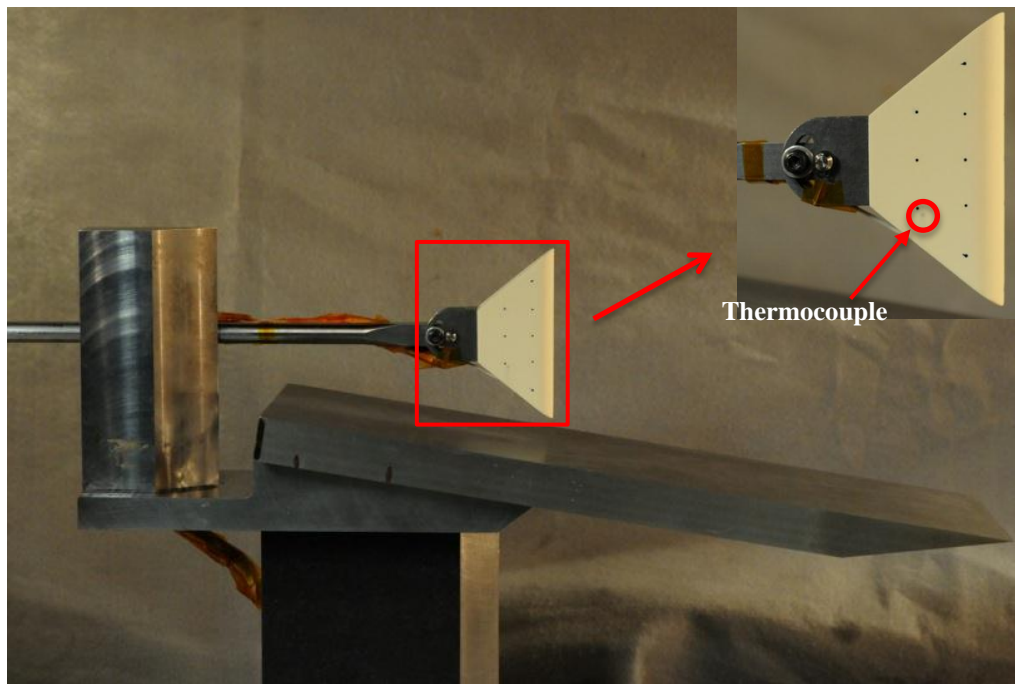


**Figure 7. Fused silica (0.50 in-radius) test article with a thermocouple near the bottom and a close-up inset image showing the thermocouple bead.**

Figure 8 shows the marked test articles, including the back-up (left column) and primary (middle column) fused silica test articles, and the metal oil-flow test articles (right column). As the figure shows, the fiducials on the primary fused silica test articles spread out during the test. One possible explanation the fiducials smeared is that the Dykem® ink used to mark the fiducial locations slightly exceeded the published shelf life of twenty-four months [29]. The right two images in Figure 8 show the 0.75 in-radius metal test article (top image), without a coating of oil, and the 0.50 in-radius fused silica test article (bottom image) inserted into the tunnel test section and illuminated with 360-nm UV light to reveal the fluorescent fiducial marks and the phosphor coating, respectively. Additional information about the test article fabrication, the data acquisition processes and the run matrix for this study is provided in [27].

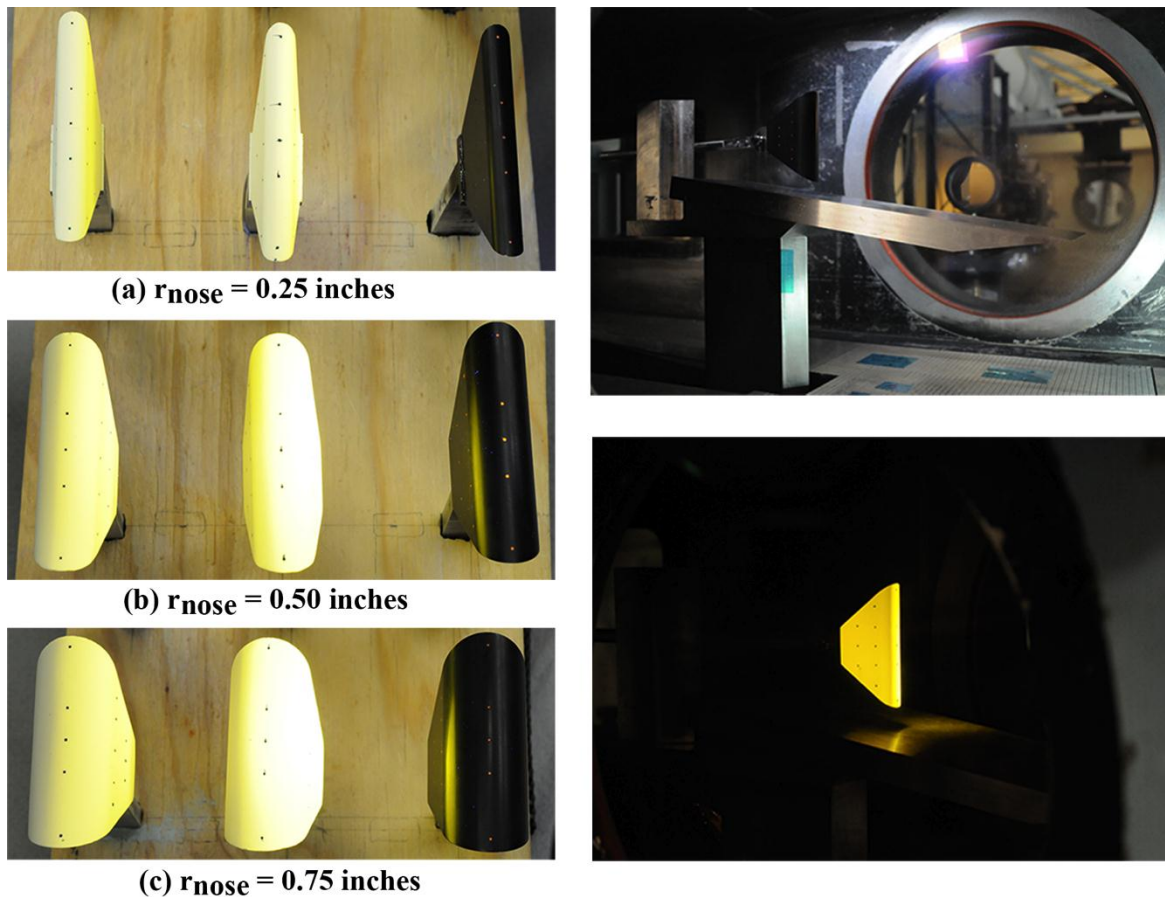


**Figure 8. Left images: Primary and back-up fused silica test articles and metal oil flow test articles. Right images: Metal test article (0.75 in-radius, top) and fused silica test article (0.50 in-radius, bottom) inserted in the tunnel with 360 nm UV illumination.**

The 20-inch Mach 6 Air Tunnel runs in Table 2 were conducted either without a SG installed or with a  $9^\circ$  SG angle. For most of these runs, the nominal Mach number was 5.96 and the Re number was  $2.1 \times 10^6/\text{ft}$ . A Re number sweep was conducted with two runs at  $1.1 \times 10^6/\text{ft}$ , one run at  $2.1 \times 10^6/\text{ft}$ , and one run at  $4.1 \times 10^6/\text{ft}$  for the 0.25 in-radius test article at a  $-15^\circ$  AoA. The test article AoA was either  $0^\circ$ ,  $-15^\circ$  or  $-25^\circ$  in each case to yield a Type IVa, a Type IV or a Type III interaction. These shock-shock interaction types were visually confirmed using high-speed schlieren data obtained using a Phantom 9 or a Phantom 12 camera. The framing rate increased from 1600 fps (Phantom 9) to 7900 fps (Phantom 12) for the runs listed in the table. The “yes/no” in the phosphor category indicates a repeated run because phosphor data was not recorded during the initial run. Phosphor thermography data was obtained both with the typical camera settings (“zoomed out” in table) and with a close-up camera view (“zoomed in”) to increase the spatial resolution of the acquired temperature data points.

Two oil-flow techniques were used to visualize the flow behavior over the surface of the metal test articles. In the first method, a clear base coat of 350 centipoise (cP) oil was applied to the test article and dots of 350 cP oil mixed with a titanium white pigment were flicked onto the surface of the test article as shown in the left image in Figure 9. The streaks produced by the dots of oil reveal the flow streamlines. The second method involved covering the test article with a full layer of the 350 cP oil mixed with pigment as the right image in Figure 9 shows. High viscosity oil was selected to reduce the loss of the pigmented oil due to high shear levels. Two techniques were implemented because the oil dot technique provides information about streamline movement, but the oil coating technique provides insight in to the regions of high shear on the test articles. Also, the size of the dots generated in the conventional technique is random, producing small dots of oil that will not move much during a wind tunnel run and large dots of oil that spread out and blur the motion of the surrounding streamlines. The full coating method is more repeatable between runs and ensures the entire surface is covered with a sufficient amount of oil to provide insight into the surface flow. Repeat runs were conducted to obtain better oil-flow streamlines or zoom schlieren videos.



**Table 2. Metal and fused silica test articles run matrix.**

Test Article	# Runs	$Re_{\infty}$ $ft^{-1} \times 10^{-6}$	SG Angle	Leading Edge AoA	Spatial Zoom	Phosphor	Schlieren
Metal, oil-flow: 0.5-in diameter	2	2.1	9°	0°	Out	No	Phantom 9
	3	2.1	9°	-15°	Out	No	Phantom 9
	2	2.1	9°	-25°	Out	No	Phantom 9
Metal, oil-flow: 1.0-in diameter	2	2.1	9°	0°	Out	No	Phantom 9
	2	2.1	9°	-15°	Out	No	Phantom 9
	2	2.1	9°	-25°	Out	No	Phantom 9
Metal, oil-flow: 1.5-in diameter	2	2.1	9°	0°	Out	No	Phantom 9
	2	2.1	9°	-15°	Out	No	Phantom 9
	4	2.1	9°	-25°	Out	No	Phantom 9
Fused silica, phosphor-coated: 0.5-in diameter	1	2.1	None	0	Out	Yes/No	Phantom 12/None
	1	2.1	None	-15	Out	Yes	None
	1	2.1	None	-25	Out	Yes	Phantom 12
	2	2.1	9°	0	In/Out	Yes	Phantom 12
	2	1.1	9°	-15	In/Out	Yes	Phantom 12
	2	2.1	9°	-15	In/Out	Yes	Phantom 12
	1	4.1	9°	-15	Out	Yes	Phantom 12
	2	2.1	9°	-25	In/Out	Yes	Phantom 12
Fused silica, phosphor-coated: 1.0-in diameter	1	2.1	None	0	Out	Yes	Phantom 12
	1	2.1	None	-15	Out	Yes	Phantom 12
	1	2.1	None	-25	Out	Yes	Phantom 12
	3	2.1	9°	0	In/Out	Yes	Phantom 12
	2	2.1	9°	-15	In/Out	Yes	Phantom 12
	2	2.1	9°	-25	In/Out	Yes	Phantom 12
Fused silica, phosphor: 1.5-in diameter	1	2.1	None	0	Out	Yes	Phantom 12
	1	2.1	None	-15	Out	Yes	Phantom 12
	1	2.1	None	-25	Out	Yes	Phantom 12
	1	2.1	9°	0	In/Out	Yes	Phantom 12
	1	2.1	9°	-15	In/Out	Yes	Phantom 12
	3	2.1	9°	-25	In/Out	Yes/No	Phantom 12

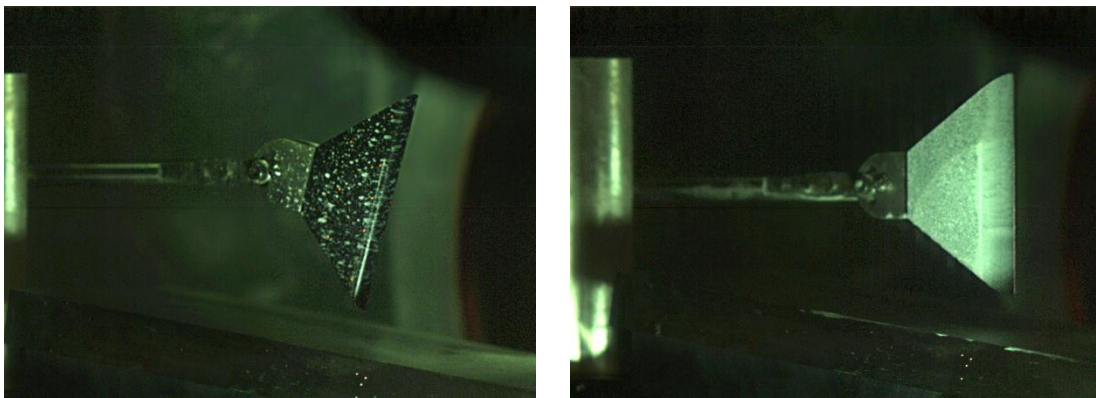


**Figure 9. Example of a metal test article covered with white oil dots (left) or full layer (right) near the beginning of the run.**

For the oil flow test, two additional cameras were used during each run. Videos of the oil flowing along the surface of the test article were recorded through the side tunnel window at a framing rate of 100 fps using a Phantom 9 camera and through the top tunnel window at 30 fps using a Hitachi camera to capture the streamline movement along the leading edge. After each oil-flow run, the test hardware was retracted from the test section and still images of the surface streamline patterns were captured with a Nikon camera.

Phosphor thermography was implemented to obtain a temporal record of surface temperatures for the test articles during the wind tunnel runs. In references [30] and [31], Merski discusses a data reduction program, IHEAT, used to obtain quantitative wind tunnel aeroheating data. This phosphor thermography method is routinely used to determine the global surface temperature distribution on hypersonic wind tunnel models. In the baseline heating cases without a shock-shock interaction, the phosphor thermography images were recorded using a Sony camera at 10 fps after the initial images were taken when the model reached the tunnel centerline. During the runs with a shock-shock interaction, the phosphor data was acquired at 30 fps (the maximum framing rate of the camera) to maximize the amount of global temperature data obtained before the leading-edge temperatures exceeded the phosphor system limit. The thermocouple data was obtained at 30 Hz.

Separate runs were conducted for each test article configuration with the phosphor camera either zoomed out to capture the full side and leading edge of the test article or zoomed in to view only the areas near the shock-shock interaction. The spatial resolution of the phosphor data ranged from 0.0105 in to 0.015 in between the acquired temperatures for the zoomed-out cases, and was about 0.004 in for the zoomed-in cases. These spatial resolutions are sufficient for the heat transfer experiments and confirm the minimum thin-film-gage spacing of 0.015 in in [15] deemed necessary to capture the narrow heating spike for Type III and IV interactions accurately.

The flow density gradients during the wind tunnel runs were recorded using a custom zoom schlieren system set up specifically for this study. Details are provided in reference [27]. Standard schlieren systems typically utilize the entire field of view available from the wind tunnel windows to acquire density gradient videos and images. Standard schlieren data was not acquired. Zoom schlieren systems use a set of lenses with a continuous light source to magnify a smaller region of interest in the flow. Zoom schlieren data was collected using different Phantom cameras as shown in the tables with increasingly higher framing rates and a variety of camera lenses over the span of the wind tunnel experiment in an attempt to obtain a clearer picture of the shock-shock interaction without blurring due to unsteadiness in the flow. Phantom 9 data obtained at 1600 fps is presented in the results section, since the contrast in the Phantom 12 images (possibly due to the lower light exposure at the higher framing rate) was frequently poor.

#### 4. Heat transfer analysis

Surface heat transfer coefficients based on the temperature readings for the fused silica test articles were calculated using IHEAT and 1D and 2D FV conduction codes. These programs were used to determine the optimum method to predict heating profiles if test articles are exposed to sharp temperature gradients, which in this study were produced by shock-shock interactions. The IHEAT code is the primary method used to analyze phosphor thermography data obtained in Langley's hypersonic facilities. IHEAT is a 1D code that assumes the test article is semi-infinite in the through-thickness dimension, so heat applied at the surface does not reach the back of the test article during a short wind tunnel run. Convective heat transfer coefficients,  $c_h$ , are calculated from a convective heat transfer,  $\dot{q}_{conv}$ , equation based on an enthalpy difference, ie.,

$$\dot{q}_{conv} = c_h(h_{aw} - h_w) \quad (1)$$

Additional assumptions and equations incorporated in the IHEAT code are described in [30] and [31].

Two direct, finite-volume codes were written in Fortran to approximate the conduction in the phosphor-coated fused silica test articles. The 1D code assumed heat was conducted only through the thickness of the test article, while the 2D code also considered conduction in the lateral direction. The purpose of the 1D FV code in the present study is to provide a direct comparison between the 1D algorithm in IHEAT and the assumptions in the FV codes for the 1D versus 2D comparison. Both the IHEAT and 1D FV codes neglect the effect of surface curvature.

The diagram in Figure 10 shows the cylindrical geometry used in the 2D code to approximate the test article leading edge. To simplify the calculations, the code assumes a cylinder with dimensions equal to the leading-edge length (4 in) and the appropriate nose radius. A rectangle bounded by the stagnation line on the leading edge and the centerline of the cylinder (in red in Figure 10) defines the boundaries of the nodes in both FV codes. The 2D code used cylindrical cell volumes that surrounded nodes in the rectangular plane. Definitions of the areas and volumes around the nodes in the 2D grid are provided in [27]. The coordinate systems in the figure apply to both FV codes.

Two boundary conditions are applied to the grid of finite volumes in the 1D code, and four boundary conditions are applied in the 2D code. A Dirichlet boundary condition is applied at the surface ( $r = R$ ) in both codes using the known temperatures,  $T_p$ , of the test articles at each time step. An adiabatic boundary condition (no heat transfer) is assumed at the cylinder centerline ( $r = 0$ ) in both codes. The boundary conditions at the top ( $z = L$ ) and at the bottom ( $z = 0$ ) of the cylinder in the lateral direction are also adiabatic in the 2D code. Adiabatic boundaries are assumed because temperature data is not available for nodes outside of the rectangular plane. Thus, the discrete heat transfer expressions that include nodal information external to the boundary nodes are assumed to be equal to zero.

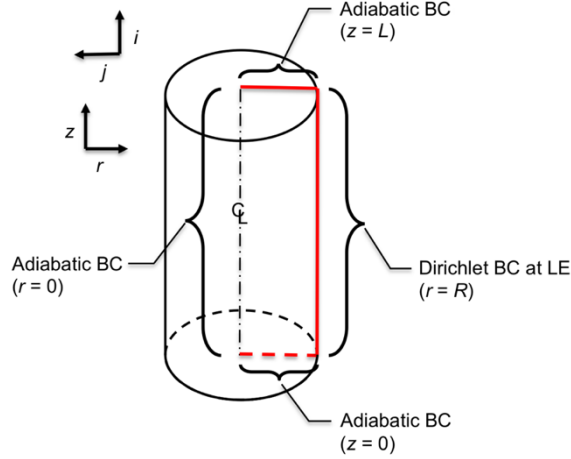


**Figure 10. Overall view of the boundary conditions of the cylindrical leading edge modeled in the 1D (neglecting curvature) and 2D (using cylindrical coordinates) FV codes.**

The 1D code uses a FV formulation of the Crank-Nicolson algorithm to solve the discretized conduction equation in the radial direction. The Crank-Nicolson method employs the trapezoidal rule of time integration in which the discrete spatial temperature gradient is evaluated as an average of the gradient at the current ( $n$ ) and future ( $n+1$ ) time steps [32]. This method yields an unconditionally stable time-marching scheme in the 1D FV code. The resulting system of equations forms a tri-diagonal system matrix that is multiplied by the temperatures at the central nodes of each cell. These equations comprise a system matrix used in the implicit Thomas Algorithm [33] to solve for the nodal temperatures.

The 2D conduction equation is discretized using a FV, unconditionally stable, alternating direction implicit algorithm [33]. This method sweeps through the geometry of the test article twice for every time step, first in the “ $z$ ” direction (along the fin leading edge) for all the nodes and then in the “ $r$ ” direction (radially) using an updated temperature distribution,  $T^*$ , at the intermediate time step ( $\Delta t/2$ ). Chapter 4 in [27] describes the equations used to approximate an initial temperature distribution and to calculate the heat transfer coefficients in the 1D and 2D codes.

The heat transfer coefficients are calculated at the end of each full time step in both the 1D and 2D FV codes. An energy balance on the stored heat and the radiation, convection, and 2D conduction heat transfer at the test article surface is given by

$$\rho c_p V \frac{\partial T}{\partial t} = \frac{\partial}{\partial r} \left( A_{cond} k \frac{\partial T}{\partial r} \right) + \frac{\partial}{\partial z} \left( A_{cond} k \frac{\partial T}{\partial z} \right) - [A_{rad} \epsilon \sigma (T_{i,j}^4 - T_{tw}^4)] - A_{conv} c_h (h_{aw} - h_w) \quad (2)$$

The variables  $A_{cond}$ ,  $A_{rad}$  and  $A_{conv}$  represent the areas through which heat is transferred by conduction, radiation, and convection, respectively. These variables vary depending on the volume  $V$  of the cell for which the heat transfer is computed. The variable  $\epsilon$  is the emissivity,  $\sigma$  is the Stefan-Boltzmann constant,  $T$  is the temperature at a given location (either at each node specified by  $i$  in the 1D code or  $i, j$  in the 2D code, or at the tunnel wall,  $tw$ ),  $h_{aw}$  is the adiabatic wall enthalpy and  $h_w$  is the enthalpy of the air at the surface temperature of the test article. The density,  $\rho$ , specific heat,  $c_p$ , and thermal conductivity,  $k$ , in the heat transfer equation are shown as constant values. In both the 1D and 2D FV conduction codes, the thermal properties of  $c_p$  and  $k$  depend on temperature and are updated after each full time step. The left side of equation (2) represents energy stored in the object due to a temporal temperature gradient,  $\partial T / \partial t$ . The right side represents heat conducted through the object due to a second-order spatial temperature gradient, either  $\partial^2 T / \partial r^2$  or  $\partial^2 T / \partial z^2$ . After the heat transfer equation is properly discretized, the equation is rearranged to solve for the enthalpy-based heat transfer coefficient,  $c_h$  for each surface volume at a non-dimensional position specified as the spatial location  $x$  (which is equal to 0 at the lower tip) at which the heat transfer coefficient divided by the full length  $L$  (4 in) of the leading edge.

The FV codes output a dimensional heat transfer coefficient based on the temperature data at each pixel along the leading edge of the test article. The 1D code loops through input data to derive a heat transfer coefficient at every pixel individually, while the 2D code calculates the data for the full leading edge using a line implicit scheme. These heat transfer coefficients are then non-dimensionalized to determine the relative magnitude of the peak heating in the

shock-interaction region compared to the baseline heating (no interaction). The heat transfer coefficients at  $x/L = 0.75$  to  $x/L = 0.85$  along the leading edge are relatively far away from both the peak heating region and the leading-edge fiducial marks. In the runs for which the full leading edge was visible in the image, these coefficients were averaged to provide a reference coefficient to derive non-dimensional data.

For some of the wind tunnel runs in which the camera is zoomed in on the shock interaction region, baseline heating data is not available. To be consistent, each zoomed-in run uses the average value from the corresponding zoomed-out run as a reference value to calculate non-dimensional data. The test article surface temperatures vary slightly between runs, so this assumption yields lower non-dimensional peak heat transfer coefficients in some of the zoomed-in cases, as evidenced by the cases in which data outside the shock interaction region is available and is less than 1.0. This assumption is necessary to compare the non-dimensional data with higher (zoomed-in) and lower (zoomed-out) spatial resolution.

A comparison in Figure 11 demonstrates the potential error associated with reducing the zoomed-in leading-edge data by a reference heat transfer coefficient from a separate wind tunnel run. If an average of the zoomed-in heat transfer data from Run 44 (between  $x/L = 0.38$  and  $x/L = 0.41$ ) is used to obtain non-dimensional heat transfer coefficients, the peak heat transfer coefficient  $c_{h}/c_{h,ref}$  is 4.3. However, if the reference value from Run 43 (averaged over  $x/L = 0.75$  to  $x/L = 0.85$ ) is used, the peak  $c_{h}/c_{h,ref}$  is only 3.5. If data in Run 44 in the region between  $x/L = 0.75$  and  $x/L = 0.85$  were available to be used for a reference, non-dimensional data from this run would likely lie somewhere between the two curves shown in the plot, since the heat transfer coefficients in the region from  $x/L = 0.38$  to  $x/L = 0.41$  are typically slightly higher than the coefficients farther up the leading edge.

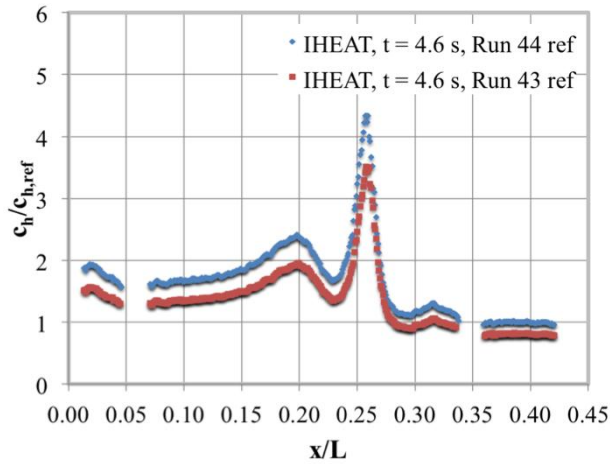


**Figure 11. Heat transfer coefficients for the zoomed-in case at  $t = 4.6$  s from the IHEAT code for the 0.25 in-radius test article at a  $-15^\circ$  AoA and a  $Re = 1.1 \times 10^6/ft$  (using two different reference values).**

## 5. Experimental measurements and results

Zoom schlieren, oil-flow and heat transfer data are presented to visualize the shock-shock interactions and to assess the effects of these flow phenomena for fins swept  $0^\circ$ ,  $-15^\circ$ , and  $-25^\circ$ . These sweep angles provide two cases with strong lateral temperature gradients due to the Type IV (at a  $-15^\circ$  AoA) and the Type III (at a  $-25^\circ$  AoA) shock-shock interaction regions, and one lower heating case for a Type IVa interaction (at a  $0^\circ$  AoA) with smaller lateral temperature gradients. These cases were selected to assess the need for a two-dimensional analysis method. Also, three test article geometries were tested to determine how the features of each type of interaction change due to the leading-edge radius. The shock-shock pattern is more clearly distinguishable in the zoom schlieren images for the 0.75 in-radius test articles since the bow shock standoff distance is greater, so the interaction is more spread out.

In the 2D schlieren images, the planar incident shock is seen as a line. The planar incident shock extends on either side of the bow shock, giving the impression that the incident shock continues through the bow shock. However, the heat transfer behavior of the shock-shock interactions suggests the incident shock does not impinge on the test article but instead wraps around the bow shock. The “incident shock impingement” described in the following images references the location where the incident shock would impinge on the leading edge in the absence of the bow shock. In computed schlieren images of the stagnation plane derived from CFD results, the incident shock does not appear to continue through the bow shock [34].

The Type III and IV interactions provided peak heat transfers that quickly exceeded the maximum phosphor thermography temperature limit. For that reason, the temperature data is reduced to heat transfer coefficients early in

the run, at a time  $t = 1.8$  s after the beginning of the test article insertion sequence that equates to the seventh frame in the recorded 30 fps data. In most cases, all the temperatures in these early line cuts were within the phosphor limits, permitting a comparison of the trends in the heat transfer coefficients due to each shock-shock interaction for the three leading-edge radii. A temporal collapse of the leading edge line cuts and an analysis of the trends in heat transfer coefficients in specific surface locations over time were used to determine when to take the line cuts, as described in [27].

The x-axis in the heat transfer plots shows the non-dimensional  $x/L$  locations. These locations are offset for the 0.50 and 0.75 in-radius test articles to align the notable features of the line cuts (either the valley for the Type IVa interaction or the peaks in the Type III and IV interactions). Gaps in the line cuts along the leading edge result from the removal of fiducial mark data. Five fiducial mark locations were used to align the test article vertically in the wind tunnel and to guarantee that at least two fiducial marks are visible when the camera is zoomed in on the interaction region. Phosphor thermography results from the current experiment are compared to thin-film data from [15]. The x-axis coordinates for the previous heat transfer plots are labeled  $x/L_{Incident Shock}$  to indicate the heat transfer coefficients are positioned relative to the extrapolated incident shock location (at  $x/L_{Incident Shock} = 0$ ) to align the data from separate wind tunnel runs.

Contour maps of the 1D Fay-Riddell [35] non-dimensionalized heat transfer coefficients from IHEAT are presented at  $t = 1.8$  s into the run. The limits on the color bar scale in each contour map are manually set between zero and three. This scale is selected to ensure the main features of the heat transfer pattern are visible for every test configuration. Although  $c_H/c_{H,FR}$  exceeds three for a few wind tunnel runs, yielding a pink (over-scaled) shock-impingement region, the basic differences between the heating patterns are distinguished in these images. Different reference values were used to convert the heat transfer contour maps and the line cuts to non-dimensional data, so the y-axis scale in the plots does not directly correlate to the color bar on the contour maps.

Based on a grid convergence study presented in [27], a grid with 1001 volumes in the radial direction ( $nr$ ) is used in the FV codes for the 0.25 in-radius test article. This number of volumes is much more than the required number to obtain a converged solution. A corresponding number of 2001 and 3001 volumes are used in the grids for the 0.50 in- and 0.75 in-radius test articles to maintain the same spacing  $\Delta r$  in the radial direction for all the test articles. The number of volumes utilized in the lateral direction ( $nz$ ) in the 2D code depends on the number of pixels for which temperatures are available for the leading edge line cut in any given run.

Uncertainties in the phosphor thermography data depend on the rise in the test article surface temperatures. The following values of uncertainty are based on historical tests with a variety of types of test articles. On surfaces with a significant temperature rise ( $>70^\circ\text{F}$ ), uncertainties are in the range of  $\pm 10\%$ . For moderate temperature increases ( $20\text{--}30^\circ\text{F}$ ), the uncertainties are roughly  $\pm 25\%$ . More information on phosphor thermography uncertainties is found in [30] and [31]. Error bars are not included in the following plots due to the density of the data in the line cuts.

The peak heat transfer coefficient in the shock-shock interaction region increases with increasing leading-edge radius in the following non-dimensional line cuts. This trend is the opposite from the peak behavior in dimensional line cuts. This reversal in the leading-edge radius effects occurs because the reference value used to convert the heat transfer coefficients to non-dimensional values decreases as the leading-edge radius increases, which amplifies the peak heat transfer value for the larger test article geometries. Non-dimensional heat transfer line cuts are presented to estimate the peak heating augmentation relative to the expected heat transfer. If a vehicle's geometry is designed to handle the predicted heat transfer levels for known hypersonic flow conditions, then the relative heating augmentation in the presence of a plausible shock-shock interaction strongly influences the design of the TPS.

### 5a. Fin sweep of $0^\circ$

Figure 12 displays schlieren images of the 0.25, 0.50, and 0.75 in-radius test articles, listed from left to right, at a  $0^\circ$  AoA. The shock interaction is so close to the incident shock in the left image that the Type IVa features are difficult to distinguish, though a close inspection reveals a very narrow supersonic jet with a shear layer turned upward. The middle image shows the incident shock is further separated from the supersonic jet and the curled-up shear layer for the 0.50 in-radius test article because the bow shock is offset further from the larger test article. The shear layer appears to attach to the surface near the location where the incident shock wraps around the test article.

The Type IVa interaction for the 0.75 in-radius test article is more spread out so the features of the interaction are easier to identify. A narrow supersonic jet extends at an angle from the triple point to the location where the bow shock is again nearly vertical, before turning to travel almost horizontally to an impingement point on the surface of the test article. A pattern of triangles that comprise the shock train formed by reflected shocks is visible near the beginning of the supersonic jet. The shear layer above this region of shock triangles curves up toward the incident shock line, as evidenced by the darker region in the density gradients, which is clearer in the videos.



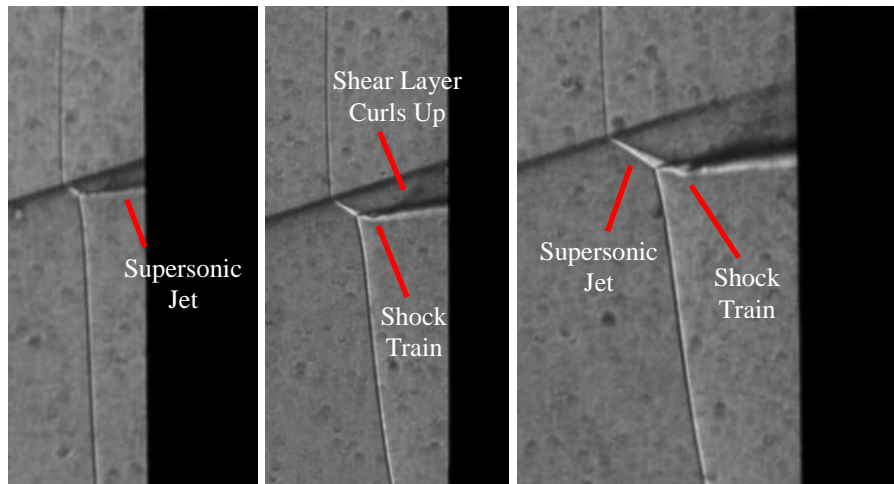


**Figure 12. Zoom schlieren images of the 0.25, 0.50 and 0.75 in-radius test articles at a 0° AoA.**

Oil flow images in Figure 13 show characteristic streamlines and shear patterns for this Type IVa interaction with the 0.75 in-radius test article. The features in these oil-flow images are similar to the streamline patterns observed in the 0.25 and 0.50 in-radius test articles. The second image from the left indicates the oil movement for a test article that was initially fully coated with oil, while the other images show streamlines on a test article that was covered with dots of pigmented oil prior to the run. Edney [1] states that a region of dead air exists along the leading edge just below the upper shear layer attachment point in an oil-flow image of a 0.59 in-radius cylinder exposed to a Type IVa interaction. The oil-flow streamlines on the leading edge in Figure 13 exhibit this same behavior. These streamlines also resemble the oil-flow streamlines for a 0.5 in-radius cylinder in [18], with different behavior near the bottom of the leading edge since the test article was separated from the flat plate SG in the current study.

Streamlines travel upward from the attachment point and then turn away from the leading edge. A horizontal line around the circumference of the leading edge in the full-coating image indicates the attachment point of the curved shear layer above the supersonic jet. This line is near the location where the planar incident shock wraps around the test article, as seen in the schlieren images. In the region near the top of the test article, the oil along the stagnation line did not move. The side oil flow patterns are similar as nearly horizontal streamlines flow away from the leading edge that turn toward the slanted edges of the test article. The bow shock around a test article at a 0° AoA is a nearly normal shock and, thus, the flow above the incident shock does not change direction but instead continues horizontally until the air reaches the surface of the test article.

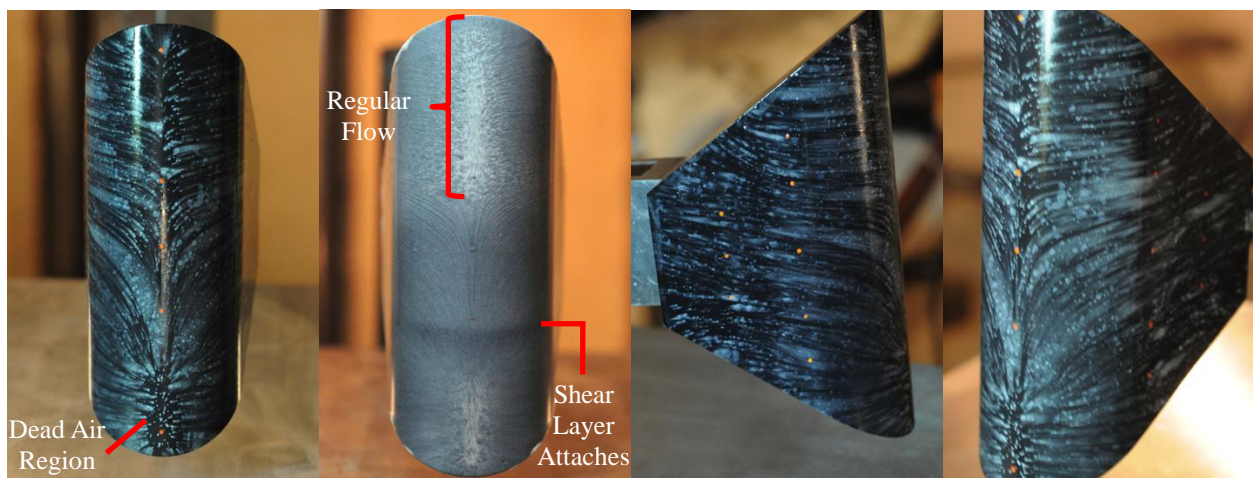


**Figure 13. Oil-flow images for the 0.75 in-radius metal test article at a 0° AoA. Numbered from left to right, 1) leading-edge view, dots, 2) leading-edge view, full coating, 3) right side view, dots, 4) left side view, dots.**

IHEAT 1D contour maps of the heat transfer coefficients show zoomed-out (Figure 14) and zoomed-in (Figure 15) views of the heat transfer coefficients on the 0.25, 0.50, and 0.75 in-radius test articles, from left to right, at a 0°

AoA. A valley in the heat transfer coefficients corresponds to a blue gap between two green regions of higher heating. This valley may be due to the “dead air” zone beneath the shear layer attachment. This region shrinks, possibly due to conduction from the high heating areas, as the leading-edge radius increases. The lower region of higher heating may be due to the flow travelling through the incident and bow shocks, and the upper region is likely due to the curved shear layer attachment. A repeat run was conducted for the 0.50 in-radius test article at a  $0^\circ$  AoA, and the heat transfer patterns were very similar between the two runs as expected [27].

The Type IVa shock interaction yielded the lowest peak heat transfer augmentation of the interactions in this study. The line cut data for all three of the test article geometries display similar features for the case with a  $0^\circ$  AoA. Two small peaks of similar magnitude exist on either side of a trough in the heat transfer coefficients along the leading edge for this type of interaction. The non-dimensional heat transfer data along the leading edge for the three test articles is presented in Figure 16. The first peak near  $x/L = 0.24$ , with  $c_h/c_{h,ref}$  approximately equal to 1.5 for the smallest test article and about 1.8 for the larger test articles, corresponds to the extrapolated incident shock impingement location on the leading edge. Below that location on the leading edge, the heat transfer is relatively constant in each case relative to the baseline heating defined as  $c_h/c_{h,ref} \approx 1$ . The shear layer above the reflected shock in this interaction attaches to the surface of the test article to produce a second peak with a maximum magnitude between 1.4 for the 0.25 in-radius test article at  $x/L = 0.36$  and 1.8 for the 0.75 in-radius test article near  $x/L = 0.43$ . The widths of the heat transfer peaks increase with increasing leading-edge radius, possibly due to conduction effects and the increased length of the shear layer prior to attachment. Edge effects yield increased heating near the tips of the test article for all three geometries. The higher heat transfer coefficients near the lower tip are due in part to the flow passing through the incident shock before the air contacts the surface of the test article.

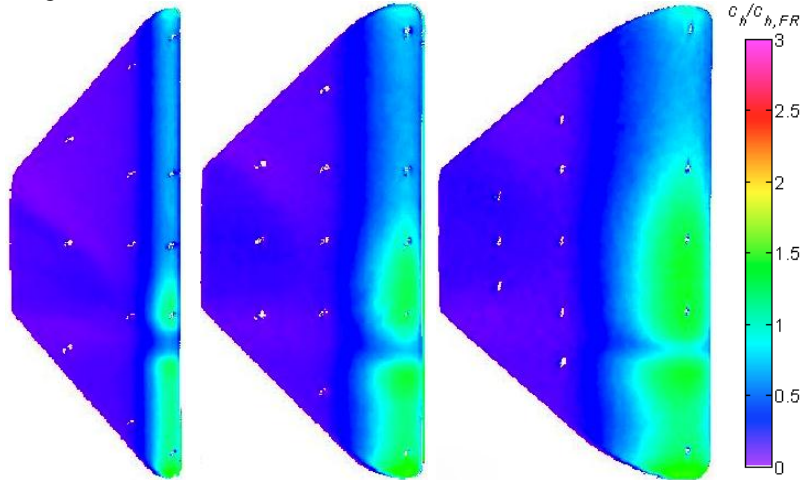


**Figure 14. IHEAT  $c_h/c_{h,FR}$  contour maps for the 0.25, 0.50, and 0.75 in-radius test articles (from left to right) at a  $0^\circ$  AoA.**

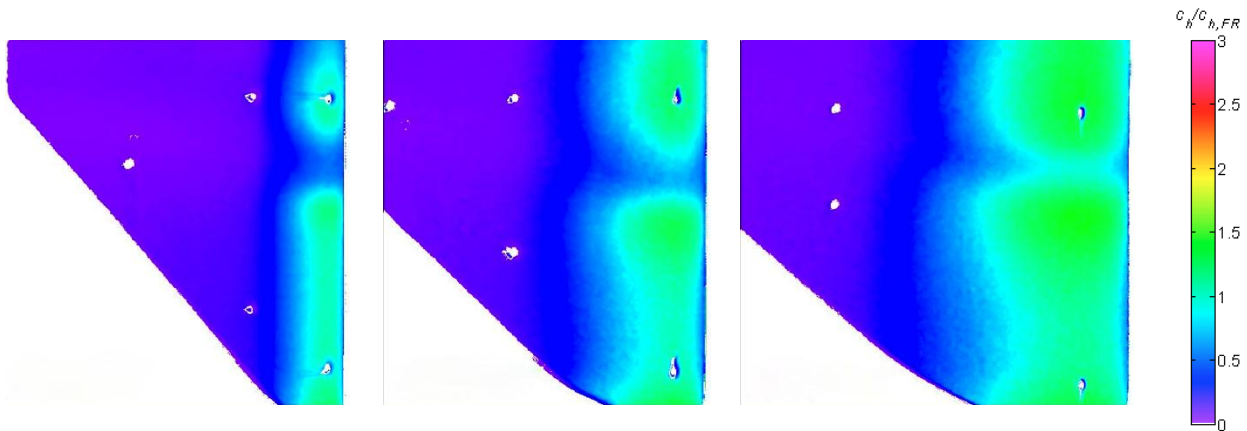


**Figure 15. IHEAT  $c_h/c_{h,FR}$  contour maps for the 0.25, 0.50, and 0.75 in-radius test articles (from left to right) at a  $0^\circ$  AoA (zoomed in).**

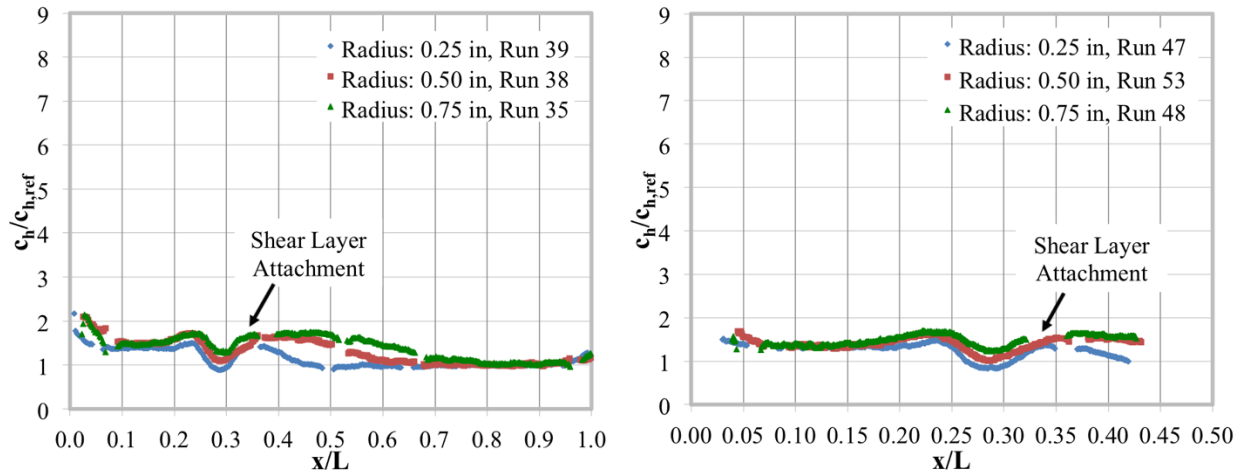


**Figure 16. Non-dimensional heat transfer coefficients from the IHEAT code for the 0.25, 0.50 and 0.75 in-radius test articles at a 0° AoA, for 1) zoomed-out (left) and 2) zoomed-in (right) data.**

Figure 17 provides historical data, taken from [15], showing the 0° AoA trends measured with thin-film gages. The Painted 1 and the Upilex® test articles names refer to different test articles, each with slightly different leading-edge resolution. The heating pattern in the Type IVa interaction data from [15] resembles the current results for the 0.25 in-radius test article. Non-dimensional heat transfer coefficients in the region exposed to flow that passed through the incident shock are relatively level near 1.5 with a peak of about 1.6 near the “incident shock impingement” location. Heating in the region above the incident shock drops slightly below 1.0 before rising to a peak of about 1.5 at the shear layer attachment point and then decreasing again to the baseline heating above the shock interaction. The increased heating near the tips of the test article in Figure 16 is not included in Figure 17 since the ends of the Painted 1 and Upilex® leading edges are not instrumented with thin-film gages.

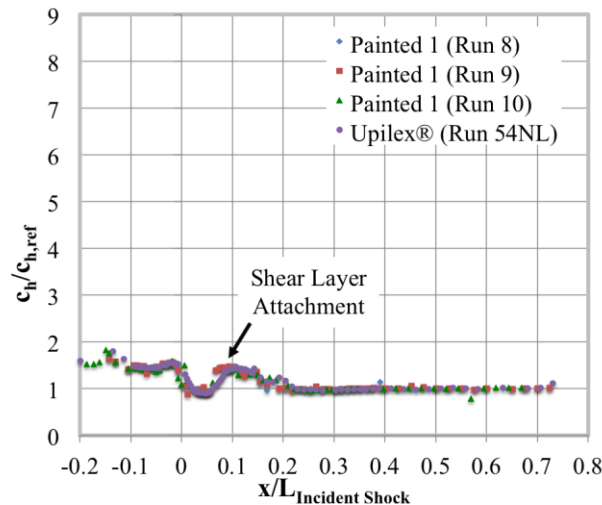


**Figure 17. Non-dimensional heat transfer coefficients from the thin-film gages on the 0.25 in-radius Macor® Painted 1 and Upilex® test articles at a 0° AoA [15].**

### 5b. Fin sweep of -15°

The characteristic features of a Type IV interaction are visible in the images for the 0.25, 0.50 and 0.75 in-radius test articles (from left to right) at a -15° AoA in Figure 18. One such feature is a supersonic jet emanating from the triple point that impinges nearly perpendicularly on the surface of the test article. The schlieren videos of this interaction reveal changes in the density of the air between the bow shock and the test article surface above the extrapolated incident shock location over time. However, the density gradient in that region is not clear in the still images in Figure 18. The shape of the bow shock above and below the interaction is similar in the images for the test articles with varying nose radii.



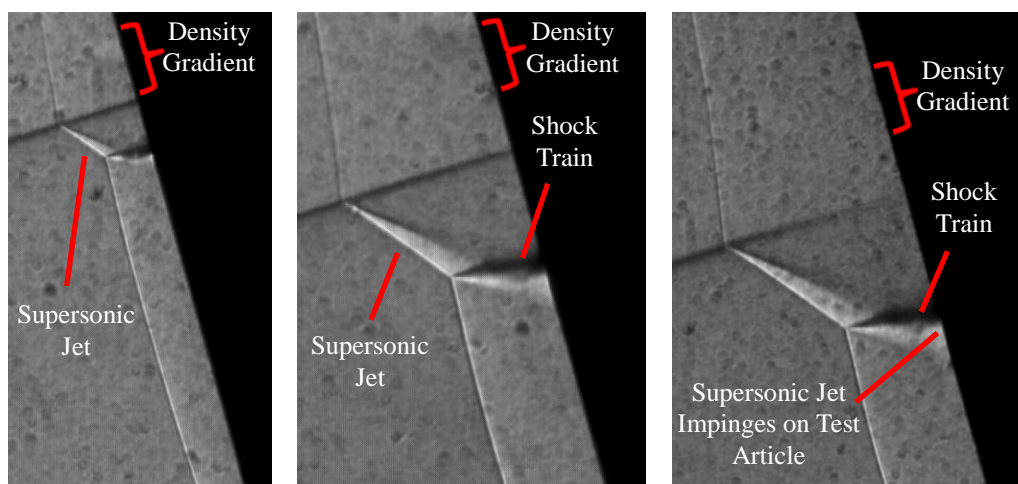


**Figure 18. Zoom schlieren images for the 0.25, 0.50 and 0.75 in-radius test articles at a  $-15^\circ$  AoA.**

Oil flow images for the 0.75 in-radius test article at a  $-15^\circ$  AoA are provided in Figure 19. These images present representative surface streamlines for a direct Type IV shock interaction. The shear associated with the supersonic jet impingement removes the majority of the oil in that region in the “full coating” images. The lower horizontal line in the two leading-edge images in this figure corresponds to the edge of this high shear region due to the supersonic jet. This line is also approximately located where the incident shock wraps around the test article (outside of the bow shock) between the two lowest fiducials on the leading edge. The lower streamlines in the left image on either side of the stagnation line resemble parabolas with a trough centered near the supersonic jet impingement. In the corresponding schlieren images, this supersonic jet impinges on the test article in a narrow horizontal region below the incident shock, perhaps driving the parabolic streamlines away from the leading edge. The upper horizontal line may be due to a vortex roll-up at the leading edge caused by two opposing flows meeting with the upper flow moving down and lower flow moving up. This vortex is seen as a density fluctuation in the schlieren videos. A region of stationary dots in the leftmost image, or an undisturbed oil coating in the second image (moving to the right), exists along the stagnation line near the top of the leading edge. The streamlines leading away from this region above the upper horizontal line indicate regular Mach 6 flow. The right two oil flow images in Figure 19 reveal side views of the same test article. A triangular shape in the middle on the side of the test article indicates the density fluctuation above the incident shock also wraps around the surface of the test article. The vortex in front of the leading edge likely continues along the sidewall but splits up into this “v-shaped” or triangular region.

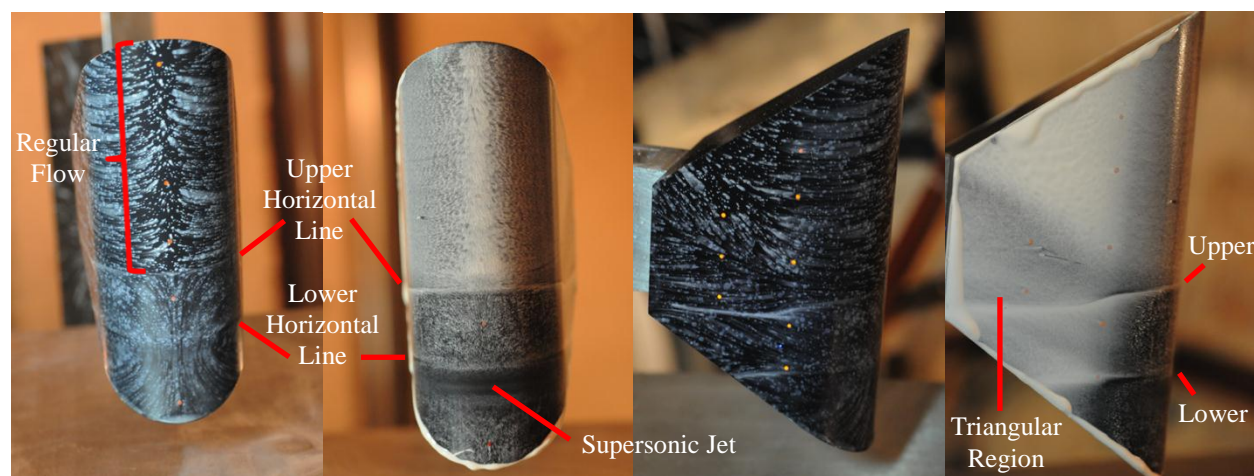


**Figure 19. Oil-flow images for the 0.75 in-radius metal test article at a  $-15^\circ$  AoA. Numbered from left to right, 1) leading-edge view, dots, 2) leading-edge view, full coating, 3) side view, dots, 4) side view, full coating.**

The contour maps in Figures 20 and 21 correspond to a Type IV interaction on the 0.25, 0.50 and 0.75 in-radius test articles, from left to right, at a  $-15^\circ$  AoA. The shock interaction wraps around the test article, creating streaks of

higher heating coefficients on the side. A narrow peak (shown in pink) on the leading edge corresponds to the supersonic jet impingement point. This peak region widens as the leading-edge radius increases. The higher heating regions spread farther parallel to and around the circumference of the leading edge as the radius increases.

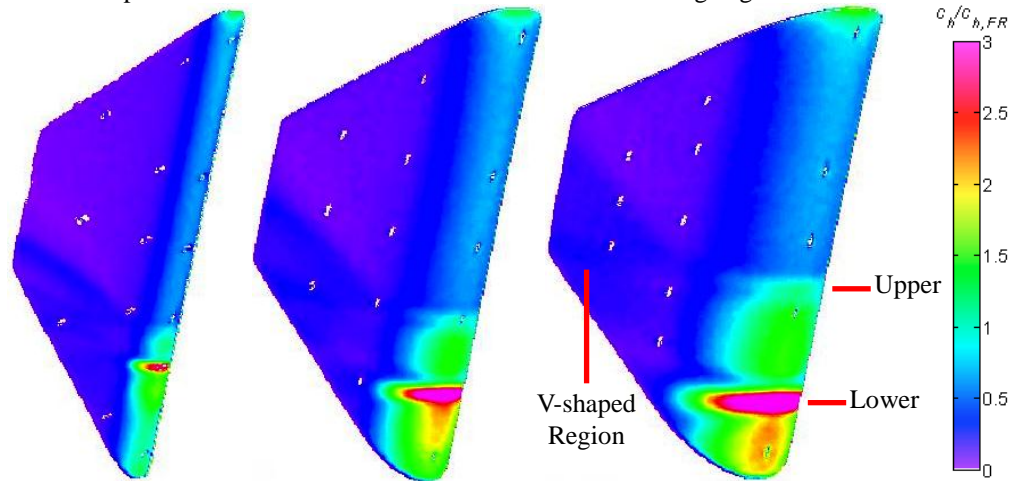


**Figure 20. IHEAT  $c_h/c_{h,FR}$  contour maps for the 0.25, 0.50, and 0.75 in-radius test articles (from left to right) at a  $-15^\circ$  AoA.**

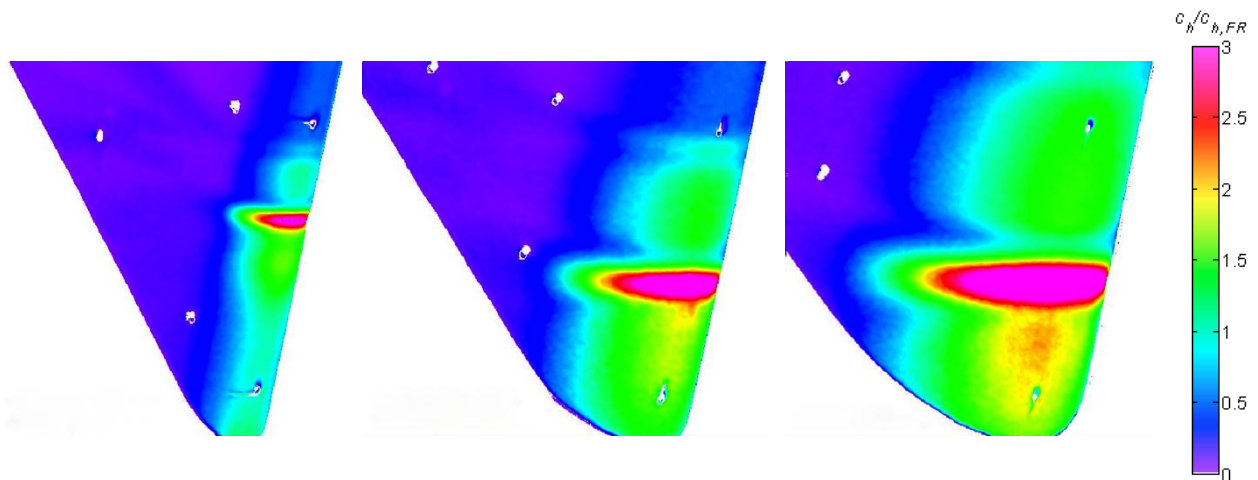


**Figure 21. IHEAT  $c_h/c_{h,FR}$  contour maps for the 0.25, 0.50, and 0.75 in-radius test articles (from left to right) at a  $-15^\circ$  AoA (zoomed in).**

The direct Type IV shock-shock interaction produces a large peak heat transfer augmentation in a narrow region as verified in the plots in Figure 22. The zoomed-in data is considered in the quantitative comparison of relative peak magnitudes since the zoomed-out peak value for the 0.25 in-radius test article exceeds the phosphor limit by  $t = 1.8$  s. A sharp narrow peak with a maximum magnitude between 4.6 for the smallest test article and about 6.8 for the largest test article indicates the impingement location of the supersonic jet at approximately  $x/L = 0.24$ . The corresponding width of the peak region ranges from approximately 0.025 non-dimensionally (or 0.1 in) to 0.06 (or 0.24 in). Two small peaks exist on either side of the peak heat transfer coefficient along the leading edge for this type of interaction for the smallest test article. The region of varying density above the incident shock in the schlieren videos, likely combined with lateral conduction effects, yields a region of increased heating that produces either a smaller peak of about 1.5 or a broader peak of about  $c_h/c_{h,ref} = 2$  to the right of the largest peak.

The heat transfer coefficients to the left of the major peak, due to flow passing through the incident shock and conduction through the test article, exceed the baseline value with a small plateau of heat transfer coefficients between 2.3 and 2.9. The increased heating at the upper tip of the test article is again evident. The shock-shock interaction moves down the leading edge as the radius increases, affecting the heat transfer to the lower tip.



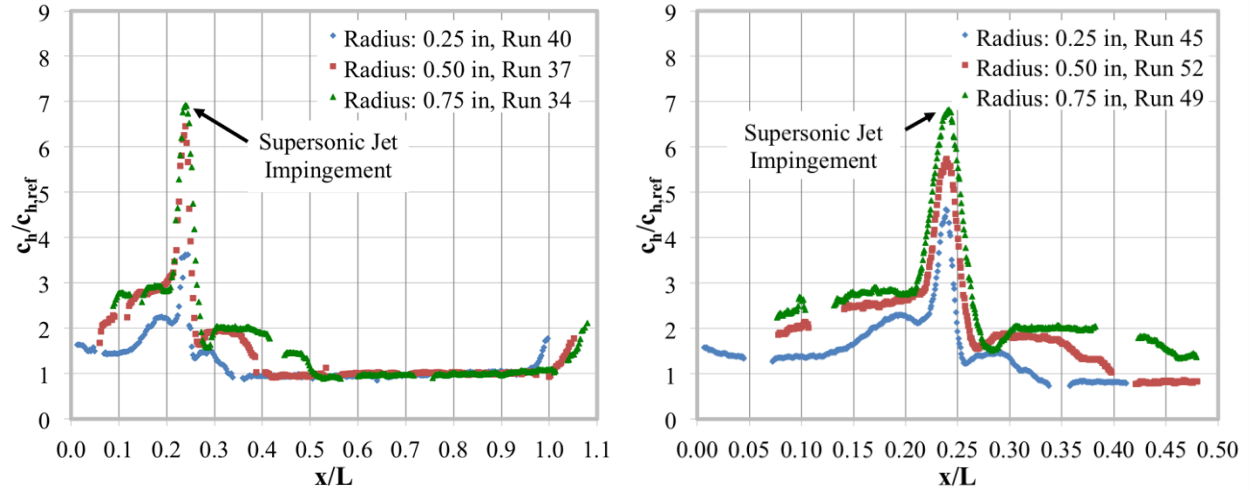


**Figure 22. Non-dimensional heat transfer coefficients at  $t = 1.8$  s from the IHEAT code for the three fused silica test articles at a  $-15^\circ$  AoA, for 1) zoomed-out (left) and 2) zoomed-in (right) data.**

Figure 23 presents the historical heating results for the direct Type IV shock-shock interaction from [15]. The Painted 1 and Upilex® thin-film data exhibit the same features of a sharp narrow peak and two smaller peaks. The maximum heating due to the supersonic jet in this case varies from 6.5 to 7. This discrepancy between the previous and current studies is possibly due to the difference in thermal properties between the fused silica substrate of the phosphor-coated test articles and the Macor® substrate of the thin-film test articles. Although the heat transfer to the test article due to the shock-shock interaction should not vary depending on which substrate material is implemented in the investigation, the surface heat transfer coefficients depend on the thermal conductivity of the test article. The peak heat transfer coefficients in the current study also are calculated at a different time in the run than in [15].

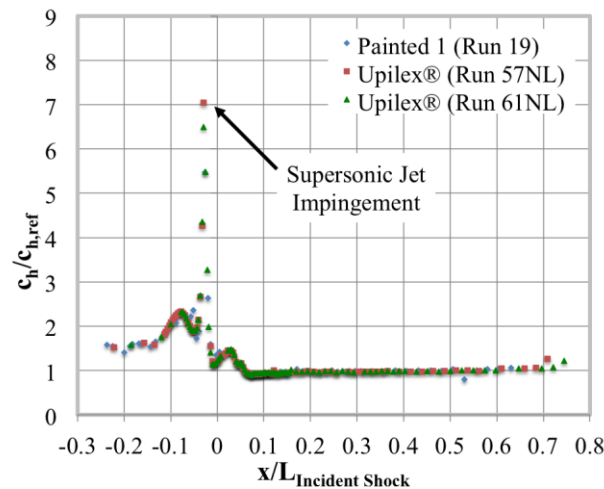


**Figure 23. Non-dimensional heat transfer coefficients from the thin-film gages on the 0.25 in-radius Macor® Painted 1 and Upilex® test articles at a  $-15^\circ$  AoA [15].**

### 5c. Fin sweep of $-25^\circ$

Figure 24 shows schlieren images (from left to right) of a Type III interaction for the 0.25, 0.50 and 0.75 in-radius test articles at a  $-25^\circ$  AoA. In the Type III interaction, the supersonic jet of the previous two interaction types is replaced with a shear layer that attaches to the surface of the test article. Supersonic flow exists in the triangular region between the turned bow shock and the shear layer in the image [1]. Although the shear layer attachment point is not clearly evident in the zoom schlieren images, the shear layer leaves the triple point with the incident and bow shocks at the appropriate angle to connect to the test article surface at the same location as the reflected shock. An unsteady region between the test article surface and the shear layer near the attachment point (labeled as a density gradient in the middle image, although this phenomenon is clearer in the schlieren videos for the three geometries)

contributes to the difficulty in capturing the shear layer attachment in a still image. As with the  $-15^\circ$  AoA case, the interaction impingement point moves down the leading edge of the test article as the leading-edge radius increases.

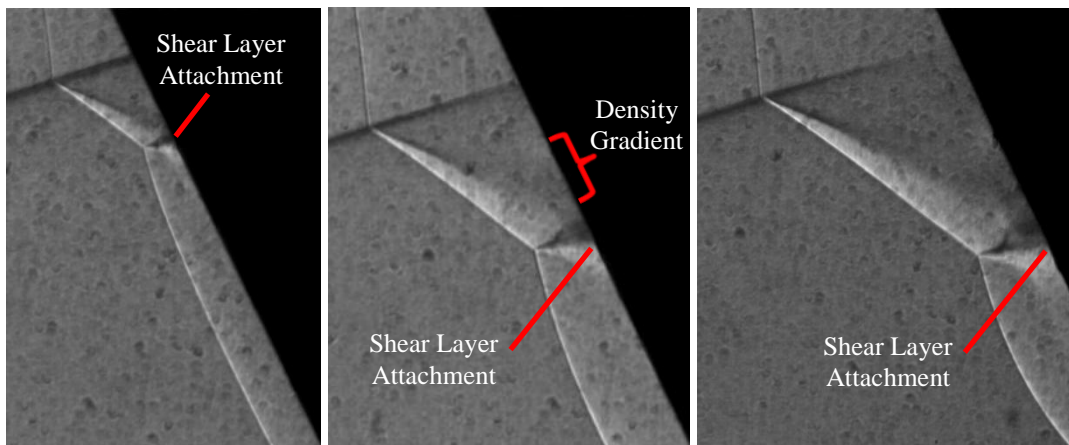


**Figure 24. Zoom schlieren (1600 fps) images for the 0.25, 0.50, and 0.75 in-radius test articles at a  $-25^\circ$  AoA.**

The Type III shock-shock interaction mainly affects the leading-edge streamlines near the extreme lower tip of the test article as shown in Figure 25 for the 0.75 in-radius test article. The streamline behavior for this test article is similar to the patterns observed on the 0.25 in- and 0.50 in-radius test articles, although the shock-interaction region occurs higher on the leading edge in those cases. The pattern in the interaction region also resembles the oil flow streamlines obtained in a Type III interaction for a 1.18 in wide flat plate in [1]. As in the  $-15^\circ$  AoA oil flow images, the streamlines near the top of the leading edge in both images follow a curved path down and out from the stagnation region. The streamlines for a  $-25^\circ$  AoA move farther downward than for the  $-15^\circ$  case, as expected, since the bow shock is angled farther forward and the flow crossing the shock turns down at a sharper angle.

The shock-interaction region produces a stagnation region below the shear layer attachment point from which the streamlines on the leading edge fan out as shown in the left leading-edge image obtained using dots of oil. The motion of the flow above and below the shear layer impingement location as demonstrated in the zoom schlieren agrees with the orientation of these streamlines. The right two oil flow images in Figure 25 were captured at an angle rather than horizontally. Thus, the line wrapping around the images near the extrapolated “incident shock” location appears to be angled downward but instead should be roughly horizontal.

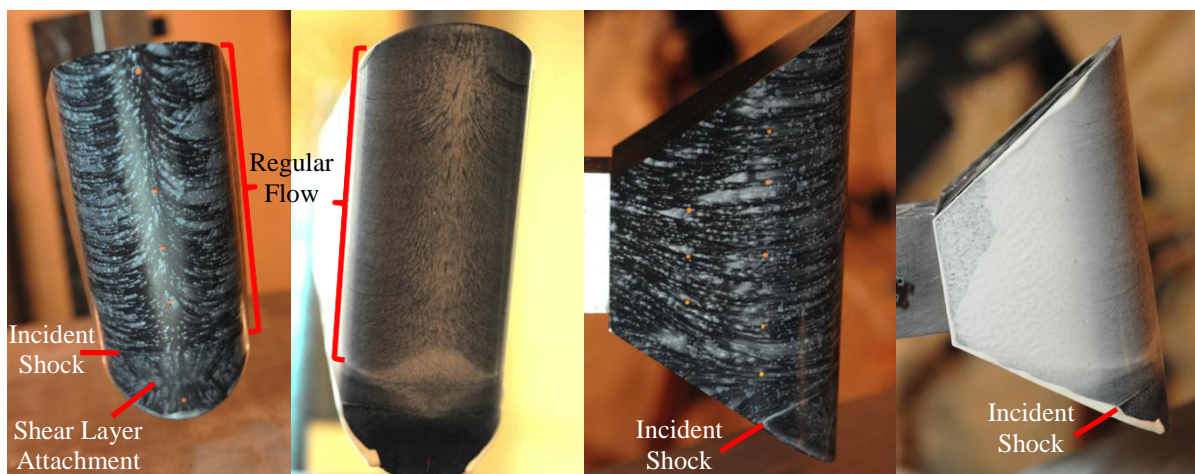


**Figure 25. Oil-flow images for the 0.75 in-radius metal test article at a  $-25^\circ$  AoA. Numbered from left to right, 1) leading-edge view, dots, 2) leading-edge view, full coating, 3) side view, dots, 4) side view, full coating.**

A Type III shock-shock interaction produces a broader peak heat transfer. Contour maps for the 0.25, 0.50 and 0.75 in-radius test articles (from left to right) at a  $-25^\circ$  AoA are included in Figures 26 and 27. The effects of the shock interaction wrap around the test article, creating streaks of higher heating. Again, the width of the peak heat

transfer region increases laterally and circumferentially with increasing leading-edge radius. The incident shock is located just above a green ellipse attached to the main peak that leads to a blue line of higher heat transfer coefficients around the side of the test article. This ellipse of elevated heating is likely due to the density gradient below the incident shock in the schlieren images and videos, which may be caused by the stagnation of the opposing streamlines along the leading edge. The flow due to the attaching shear layer moves up and the undisturbed flow above the interaction moves down, as the numerical schlieren images and video in [34] demonstrate.

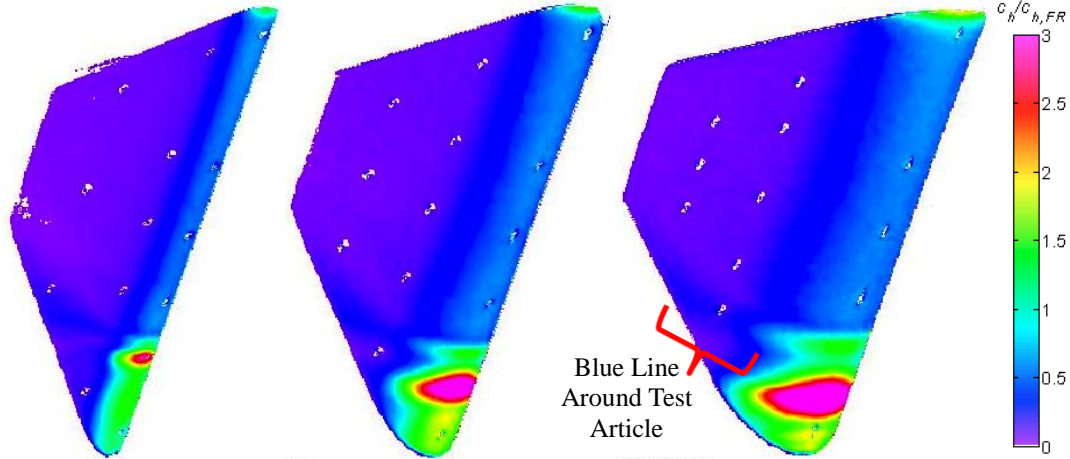


**Figure 26.** IHEAT  $c_h/c_{h,FR}$  contour maps for the 0.25, 0.50, and 0.75 in-radius test articles (from left to right) at a  $-25^\circ$  AoA.

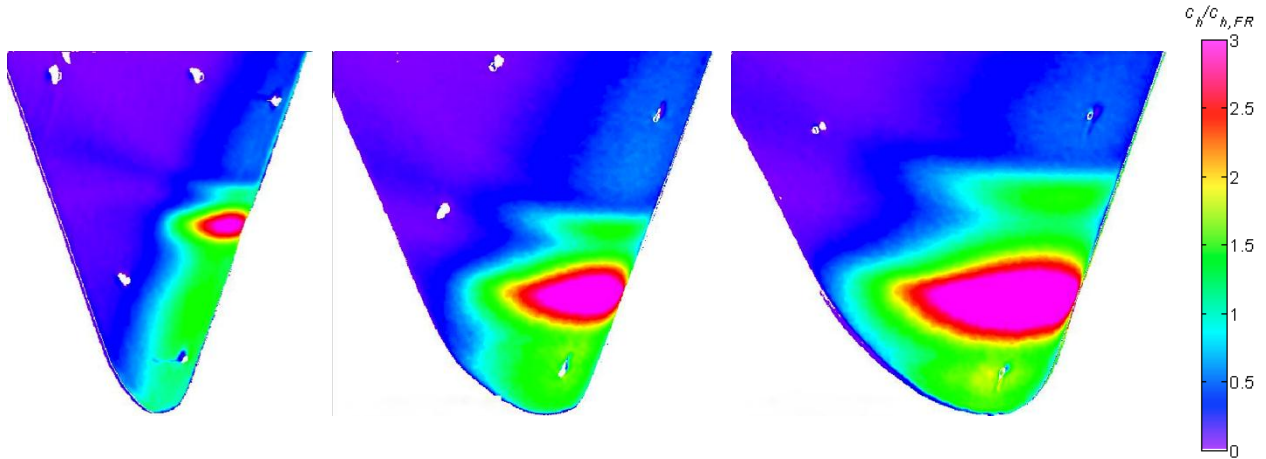


**Figure 27.** IHEAT  $c_h/c_{h,FR}$  contour map for the 0.25, 0.50, and 0.75 in-radius test articles (from left to right) at a  $-25^\circ$  AoA (zoomed in).

The zoomed-in plot in Figure 28 shows a peak at the shear layer attachment point (at  $x/L = 0.22$ ) with a width of 0.065 (0.26 in) and a maximum value of at least 5.2 for the 0.25 in-radius test article. Again, the actual peak is not calculated for the zoomed-out line cut in this case since the maximum temperature exceeds the phosphor limit at  $t = 1.8$  s. The width and the maximum value of the peak due to the shear layer attachment point increase to 0.14 non-dimensionally (or 0.55 in) and 7.9, respectively, for the 0.75 in-radius test article.

The heat transfer to the lower portion of the leading edge is about twice the baseline heating for the smallest test article, and higher for the larger ones. Warmer air that has passed through the incident shock may be partially responsible for this heating, as well as conduction through the test article. Since the angle of the shear layer relative to the incident shock for a Type III interaction only varies by a few degrees between the three test article geometries, the shear layer attachment point moves down the leading edge as the bow shock standoff distance increases and produces a greater distance between the triple point and the surface of the test article. Therefore, the region of peak heating moves closer to the lowest fiducial mark as the leading-edge radius increases for a Type III interaction, as expected from the zoom schlieren images.

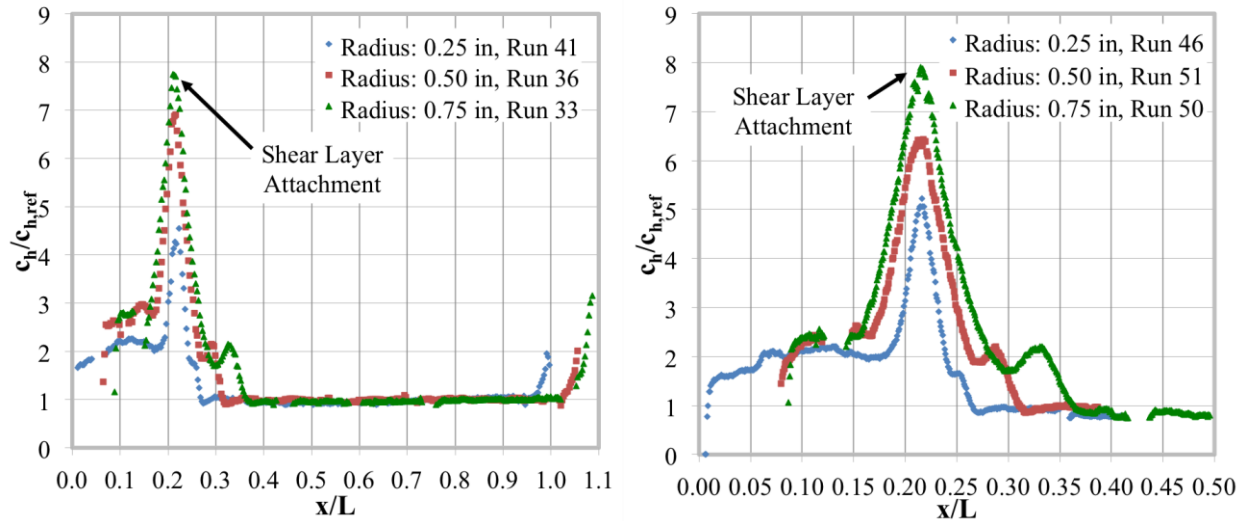


**Figure 28. Non-dimensional heat transfer coefficients at  $t = 1.8$  s from the IHEAT code for the three fused silica test articles at a  $-25^\circ$  AoA, for 1) zoomed-out (left) and 2) zoomed-in (right) data.**

Figure 29 presents historical Type III interaction data from reference [15] for the 0.25 in-radius Painted 1 and Upilex® test articles at a  $-25^\circ$  AoA. The shape of this heat transfer data is similar to the results from the current study. In both plots, a small peak near the incident shock location exists to the right of the large peak due to the shear layer attachment. The average value of the non-dimensional heat transfer to the lower portion of the leading edge is around 2 before the heat transfer coefficients decrease as in the data from the current study.

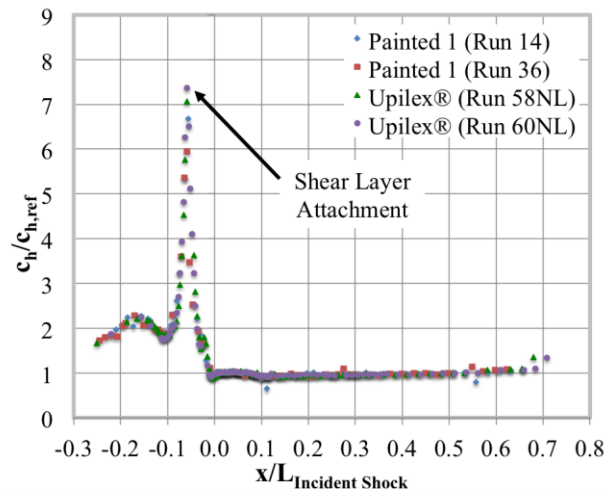


**Figure 29. Non-dimensional heat transfer coefficients from the thin-film gages on the 0.25 in-radius Macor® Painted 1 and Upilex® test articles at a  $-25^\circ$  AoA [15].**

Additional information about the magnitude and location of the peaks and valleys in the line cuts is in [27]. For example, a Reynolds number sweep was conducted to determine the impact of the Reynolds number on the peak heating due to the Type IV interaction. Also, 1D FV data is provided to compare to the IHEAT results for each case.

#### **5d. 1D versus 2D Heat Transfer**

Temperature data obtained in a run with a flow unit Re number of  $1.1 \times 10^6/\text{ft}$  was used to compute leading-edge heat transfer coefficients to provide a comparison between 1D and 2D heat transfer analyses. These heat transfer coefficients are calculated at frames 102 and 138 later in the run. Phosphor thermography data from the LAL is typically reduced using IHEAT at or near these two frames.

The plots in Figure 30 and Figure 31 show enthalpy-based dimensional (left) and non-dimensional (right) heat transfer coefficients along the leading edge of a 0.25 in-radius test article at a  $-15^\circ$  AoA at times 3.4 s and 4.6 s into



Run 43, respectively. The input data to the FV codes for this run was changed from every frame to every sixth frame (0.2 s apart) of the recorded surface temperature data obtained during Run 43. The radial spacing is  $\Delta r = 2.5 \times 10^{-4}$  in between nodes. Data is extracted from 358 pixels along the leading edge, so the lateral spacing is  $\Delta z = 1.12 \times 10^{-2}$  in.

The dimensional heat transfer coefficients derived using a 2D method which are away from the shock-interaction region on the leading edge are lower than those calculated by either 1D method. This trend is reasonable since the 2D code accounts for lateral conduction, thereby reducing the heat assumed to travel in the radial direction since heat also moves to either side of the cell in the lateral direction. The peak heating augmentation due to the supersonic jet impingement is narrower and higher for the 2D case than for the 1D cases. For the dimensional line cuts, at  $t = 3.4$  s into the run, the 2D FV peak heat transfer is about 16% greater than the peak value from IHEAT. The 2D FV non-dimensional peak heat transfer coefficient is approximately 38% higher than the corresponding IHEAT peak value. The non-dimensional coefficients away from the peak value collapse on top of each other, suggesting the offset from the IHEAT output due to the 1D and 2D FV methods is uniform in those regions.

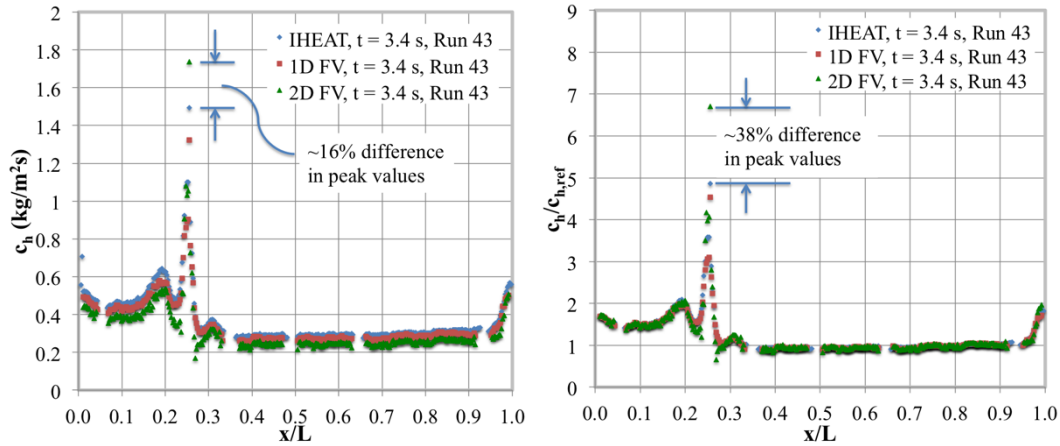


**Figure 30. Dimensional (left) and non-dimensional (right) heat transfer coefficients from the IHEAT, 1D, and 2D FV codes at  $t = 3.4$  s for the 0.25 in-radius test article at a  $-15^\circ$  AoA and a  $Re = 1.1 \times 10^6/\text{ft}$ .**

The maximum value of the y-axis of the dimensional plot in Figure 31 is only 1.4 to better show the differences between the line cuts. In this plot, the 2D peak heat transfer is about 20% greater than the IHEAT result. As expected, the difference between the IHEAT and 2D outputs increases later in the run due to errors associated with neglecting the lateral conduction and the semi-infinite assumption in IHEAT. Again, the difference between the heat transfer peaks for the 2D and IHEAT codes increases when the heat transfer coefficients are divided by a reference value to yield non-dimensional data. In the non-dimensional plot, the 2D FV peak heat transfer augmentation is about 47% higher than the IHEAT peak value. Berry and Nowak [15] predicted a non-dimensional peak heating augmentation in the Type IV interaction produced by a  $-15^\circ$  AoA for a  $Re = 2.1 \times 10^6/\text{ft}$  would increase 43%, from about 7 to 10, if lateral conduction effects were considered in the heat transfer analysis.

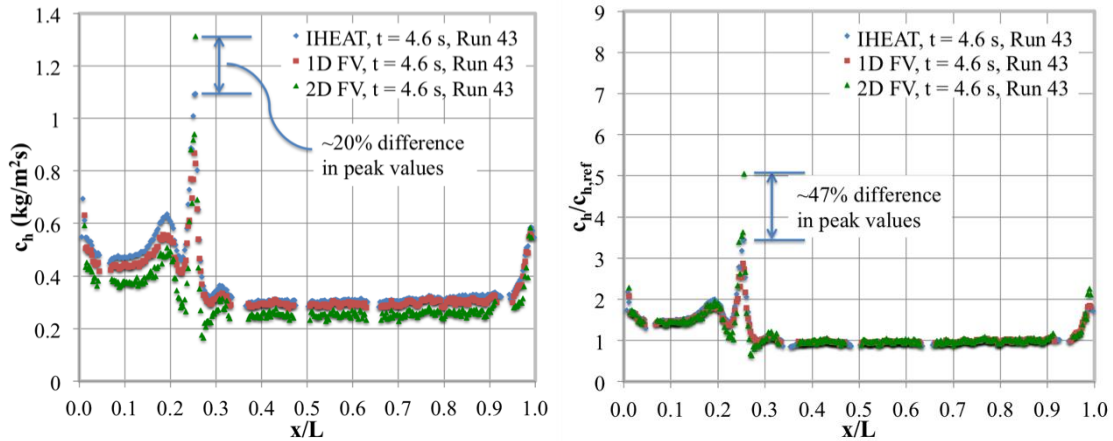


**Figure 31. Dimensional (left) and non-dimensional (right) heat transfer coefficients from the IHEAT, 1D, and 2D FV codes at  $t = 4.6$  s for the 0.25 in-radius test article at a  $-15^\circ$  AoA and a  $Re = 1.1 \times 10^6/\text{ft}$ .**



Temperature data is also available along the entire leading edge near the end of the wind tunnel runs for the lower heating cases. Thus, the 2D FV code was implemented using the temperature data at  $t = 4.6$  s for the 0.75 in-radius test article at a  $0^\circ$  AoA to compare to the 1D IHEAT results. This comparison is shown for non-dimensional heat transfer coefficients in Figure 32. The greatest difference between the 1D and 2D results is at the valley between the extrapolated incident shock location and the shear layer attachment points. In the non-dimensional heat transfer coefficients, the 2D FV value for the minimum heat transfer coefficient in this valley is about 12% lower than the minimum IHEAT value. The 1D and 2D heat transfer coefficients are similar away from the valley.

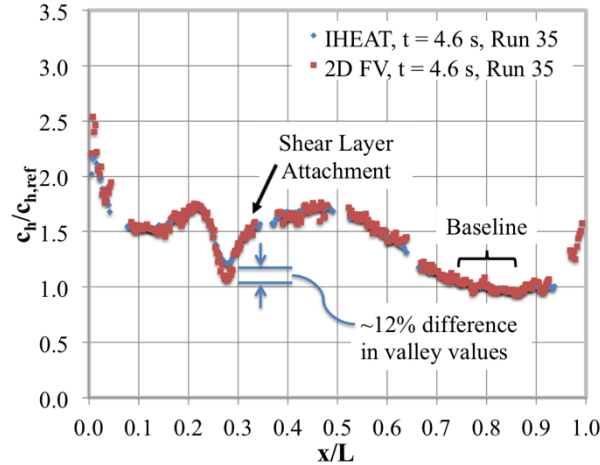


**Figure 32. Non-dimensional heat transfer coefficients at  $t = 4.6$  s from the IHEAT and 2D FV codes for the 0.75 in-radius test article at a  $0^\circ$  AoA.**

#### 5e. Spatial Resolution

The plot in Figure 33 shows a comparison of the peak region between the non-dimensional heat transfer coefficients for the zoomed-in and zoomed-out runs with a  $-15^\circ$  AoA and a  $Re = 1.1 \times 10^6/ft$ . The x-axis positions for the zoomed-in data were shifted by a small amount to better align the peak location between the two runs. As the data in the plot indicates, the spatial resolution of the zoomed-in data is about 3.8 times greater than the resolution for the zoomed-out heat transfer data. The maximum spacing between consecutive data points in a line cut for the zoomed-out data is 0.015 in, compared to about 0.004 in for the zoomed-in data. Both spatial resolutions from this global thermal imaging technique are sufficient to capture the peak heat transfer due to the shock-shock interaction. Thus, the increased resolution of the zoomed-in data provides additional confidence that the observed trends in the zoomed-out data properly represent the heat transfer behavior for each shock-shock interaction.

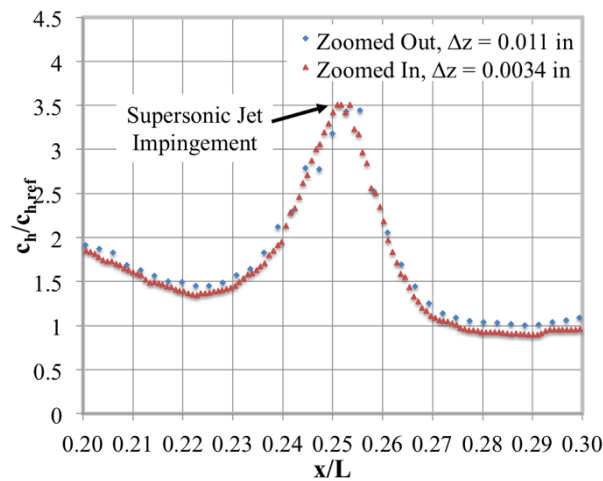


**Figure 33. Spatial resolution of IHEAT zoomed-in versus zoomed-out non-dimensional peak heat transfer coefficients at  $t = 4.6$  s for the 0.25 in-radius test article at a  $-15^\circ$  AoA and a  $Re = 1.1 \times 10^6/ft$ .**

## 6. Conclusions

The Type IVa ( $0^\circ$  AoA), direct Type IV ( $-15^\circ$  AoA), and Type III ( $-25^\circ$  AoA) shock-shock interactions were investigated using three test article geometries with leading edge radii of 0.25 in, 0.50 in, and 0.75 in, respectively. Flow density gradients were observed using a zoom schlieren technique and the surface flow was visualized using oil flow methods. The general heating behavior for these three interactions were assessed using 1D IHEAT contour maps. The leading-edge heat transfer coefficients were analyzed for each run using 1D semi-infinite and finite-volume methods and (for two cases) using a 2D finite-volume method.

Walker and Scott [20] and Wright et al. [2] recommend a greater spatial resolution than 0.015 in between gages to experimentally resolve the heat transfer peak for the Type IV interaction. The spatial resolution of the phosphor thermography data ranges from 0.004 in to 0.015 in. Therefore, the data resolution is better than or comparable to the discrete temperature gage spacing on test articles utilized in previous shock-shock interaction studies. This improved spatial resolution is significant because the heat transfer data from these line cuts display similar trends to equivalent cases in [15], confirming the assertion in [15] that a 0.015 in gage spacing is sufficient to accurately capture the narrow peak heat transfer augmentation due to a Type IV interaction. The zoomed-in line cut data yielded lower than expected results for the non-dimensional peak heat transfer data in several cases, likely due to the limitation on the reference values used to convert the heat transfer data for these runs to non-dimensional values.

Based on these observations, the Type IVa shock-shock interaction exhibits the smallest peak heating augmentation. The Type IV interaction produces a narrow, steep heat transfer peak due to an impinging supersonic jet. The Type III interaction does not include a supersonic jet as in the other two cases, but instead yields a broader peak in the heat transfer coefficients at the shear layer attachment point. Qualitatively, the heat transfer profiles from this study are similar to the corresponding Type III and IV cases in [15].

The non-dimensional peak heat transfer for a given type of shock-shock interaction increases as the leading-edge radius increases, and the dimensional heat transfer coefficients follow the opposite trend. As the leading-edge radius increases, the baseline heat transfer coefficients away from the shock-shock interaction region decrease. This trend yields a lower averaged reference value for the larger test articles, which amplifies the non-dimensional peak heat transfer augmentation compared to the smaller test article geometries.

Dimensionally, the peak heat transfer coefficient from a 2D finite-volume analysis was approximately 20% higher than the result from a 1D semi-infinite for a Type IV interaction, which corroborates the findings in [20] for a shock-shock interaction case and in [22] for striation heating due to streams of injected gas. The non-dimensional peak heat transfer augmentation calculated for a Type IV interaction at a  $Re = 1.1 \times 10^6/\text{ft}$  using a 2D ADI method is about 47% higher than the value predicted using the 1D semi-infinite IHEAT code at a point 4.6 s into the run. Berry and Nowak [15] predicted a similar non-dimensional peak heating augmentation for a  $Re = 2.1 \times 10^6/\text{ft}$  would increase 43% from about 7 to 10 if lateral conduction effects were considered in the heat transfer analysis. This difference between 1D and 2D heat transfer results is a reasonable estimate if the results for the  $Re = 1.1 \times 10^6/\text{ft}$  case can be extrapolated to a  $Re = 2.1 \times 10^6/\text{ft}$  case. For the Type IVa interaction with smaller heating gradients in the lateral direction, the difference between the 1D and 2D results was likewise smaller. Thus, a multi-dimensional conduction analysis is necessary to account for lateral conduction in cases with large temperature gradients.

## 7. Future work

The current research can be expanded and improved in the following ways. Additional comparisons between the 1D and 2D heat transfer analyses in this study require temperature data in the peak interaction region between three and four seconds into the wind tunnel runs. With the current phosphor thermography data, the 2D code can be utilized only for the  $Re = 1.1 \times 10^6/\text{ft}$  cases or the wind tunnel runs with a test article at a  $0^\circ$  AoA. In the other runs, the test article surface temperatures in the shock-interaction region exceed the maximum phosphor limit early in the run. Therefore, a new phosphor system that can sense higher temperatures is necessary to measure later temperatures in the interaction region. Currently a higher-temperature phosphor system is being developed, but this phosphor was not available at the time of the test. An infrared system with a resolution of at least  $640 \times 480$  pixels, to measure the narrow peaks for the Type IV interactions, also would be sufficient to obtain this temperature data.

One planned improvement to the 2D code is to change the geometry subroutine to accommodate additional shapes beyond a cylindrical leading edge. The 2D code also may be expanded to a 3D analysis method by switching from the ADI method to the Douglas-Gunn algorithm and implementing a 3D mapping program to directly correlate the heat transfer data to the test article geometry.

## References

- 1 Edney, Barry. *Anomalous Heat Transfer and Pressure Distributions on Blunt Bodies at Hypersonic Speeds in the Presence of an Impinging Shock*. The Aeronautical Research Institute of Sweden, Stockholm, 1968.

- 2 Wright, M. J., Nowak, R. J., Berry, S. A., Glass, C. E., and Candler, G. V. Numerical/Experimental Investigation of 3-D Swept Fin Shock Interactions. (Albuquerque, NM June 1998), AIAA 1998-2816.
- 3 Andreadis, Dean. *Scramjet Engines Enabling the Seamless Integration of Air & Space Operations*. Pratt & Whitney, West Palm Beach, FL.
- 4 NASA "Hyper-X" Program Demonstrates Scramjet Technologies. NASA Dryden Flight Research Center. [updated Dec 2009, cited Mar 2013]. URL: <http://www.nasa.gov/centers/dryden/news/FactSheets/FS-040-DFRC.html>.
- 5 La Rue, Maj. Nori. *NASA X-43A Rockets to Mach 9.8 at Edwards*. Air Force Flight Test Center Public Affairs [online resource], Edwards, CA, [updated Nov 2004, cited Mar 2013]. URL: <http://www.af.mil/news/story.asp?id=123009242>.
- 6 Barnstorff, Kathy. *X-51A Makes Longest Scramjet Flight*. NASA Langley Research Center [online resource], Hampton, VA, [updated May 2010, cited Mar 2013]. URL: <http://www.nasa.gov/topics/aeronautics/features/X-51A.html>.
- 7 Berger, Karen T., Rufer, Shann J., Kimmel, Roger, and Adamczak, David. Aerothermodynamic Characteristics of Boundary Layer Transition and Trip Effectiveness of the HIFiRE Flight 5 Vehicle. (San Antonio, TX 2009), AIAA 2009-4055. June 22-250.
- 8 Nowak, R., Holden, M., and Wieting, A. Shock/shock interference on a transpiration cooled hemispherical model. (Seattle, WA June 1990), AIAA 1990-1643.
- 9 Stewart, James R., Thareja, Rajiv R., Wieting, Allan R., and Morgan, Ken. Application of Finite Element and Remeshing Technique to Shock Interference on a Cylindrical Leading Edge. (Reno, Nevada 1988), AIAA 1988-0368.
- 10 Wieting, A. Shock interference heating in scramjet engines. (Orlando, FL October 1990), AIAA 1990-5238.
- 11 Vemaganti, G. and Wieting, A. Application of a Finite Element Algorithm for High Speed Viscous Flows Using Structured and Unstructured Meshes. (Seattle, WA June 1990), AIAA 1990-1648.
- 12 Watts, Joe D. *Flight Experiment with Shock Impingement and Interference Heating on the X-15-2 Research Airplane*. Washington D.C., 1968.
- 13 Harwood, William. *Board Hearing Shows Work to Piece Together Known Data*. Spaceflight Now Inc. [online resource]. [updated Mar 2003, cited Mar 2013]. URL: <http://www.spaceflightrightnow.com/shuttle/sts107/030318hearing/>.
- 14 Gehman, Harold W. *Columbia Accident Investigation Board Report, Vol. 3, Appendix E.2*. Government Printing Office, Washington, D. C., Aug 2003. pp. 53-55.
- 15 Berry, Scott A. and Nowak, Robert J. Fin Leading-Edge Sweep Effect on Shock-Shock Interaction at Mach 6. *Journal of Spacecraft and Rockets*, 34, 4 (July-August 1997), 416-425.
- 16 Bushnell, Dennis M. *Interference Heating on a Swept Cylinder in Region of Intersection with a Wedge at Mach Number 8*. NASA, Washington, D.C., 1965.
- 17 Keyes, J. W. and Hains, F. D. *Analytical and Experimental Studies of Shock Interference Heating in Hypersonic Flows*. Washington D.C., May 1973.
- 18 Hiers, Robert S. and Loubsky, William J. *Effects of Shock-Wave Impingement on the Heat Transfer on a Cylindrical Leading Edge*. NASA, Washington, D.C., 1967.
- 19 Carter, Howard S. and Carr, Robert E. *Free-Flight Investigation of Heat Transfer to an Unswept Cylinder Subjected to an Incident Shock and Flow Interference from an Upstream Body at Mach Numbers up to 5.50*. NASA Langley Research Center, Washington, D.C., 1961.
- 20 Walker, D. Greg and Scott, Elaine P. The Effects of Lateral Conduction on Heat Flux Estimation from Surface Temperature Measurements. *AIAA/A.S.M.E. Joint Thermophysics and Heat Transfer Conference*, 3 (June 1998), 245-252.
- 21 Walker, D. Greg. *Estimation of Unsteady Nonuniform Heating Rates from Surface Temperature Measurements*. Virginia Tech, Blacksburg, VA, 1997.
- 22 Daryabeigi, K., Berry, S. A., Horvath, T. J., and Nowak, R. J. Finite Volume Numerical Methods for Aeroheating Rate Calculations from Infrared Thermographic Data. *Journal of Spacecraft and Rockets*, 43, 1 (January-February 2006), 54-62.

- 23 Micol, J. R. Langley Aerothermodynamics Facilities Complex: Enhancements and Testing Capabilities. (Reno, NV Jan. 1998), AIAA 1998-0147.
- 24 Rhode, Matthew N. and DeLoach, Richard. Hypersonic Wind Tunnel Calibration Using the Modern Design of Experiments. (Tucson, AZ 2005), AIAA 2005-4274.
- 25 Rufer, Shann J. and Berridge, Dennis C. Pressure Fluctuation Measurements in the Langley 20-Inch Mach 6 Wind Tunnel. ( 2012), AIAA 2012-3262.
- 26 Hollis, Brian R. and Collier, Arnold S. Turbulent Aeroheating Testing of Mars Science Laboratory Entry Vehicle. *Journal of Spacecraft and Rockets*, 45, 3 (2008), 417-427.
- 27 Jones, Michelle L. *Experimental Investigation of Shock-Shock Interactions over a 2-D Wedge at  $M = 6$* . Virginia Polytechnic Institute and State University, Hampton, VA, 2013.
- 28 Buck, G. M., Powers, M. A., Griffith, M. S., Hopkins, J. W., Veneris, P. H., and Kuykendoll, K. A. *Fabrication of 0.0075-Scale Orbiter Phosphor Thermography Test Models for Shuttle RTF Aeroheating Studies*. Hampton, Virginia, November 2006.
- 29 Patel, Naresh. January 14, 2103. personal communication.
- 30 Merski, N. R. Global Aeroheating Wind-Tunnel Measurements Using Improved Two-Color Phosphor Thermography Method. *Journal of Spacecraft and Rockets*, 36, 2 (March-April 1999), 160-170.
- 31 Merski, N. R. Reduction and Analysis of Phosphor Thermography Data with the IHEAT Software Package. ( 1997), AIAA 1998-0712.
- 32 Burden, Richard L. and Faires, J. Douglas. *Numerical Analysis: Eighth Edition*. Thomson, Brooks/Cole, Belmont, CA, 2005.
- 33 Tannehill, John C., Anderson, Dale A., and Pletcher, Richard H. *Computational Fluid Mechanics and Heat Transfer, Second Edition*. Taylor & Francis, Philadelphia, PA, 1997.
- 34 Jones, Michelle L. and Mazaheri, Alireza. Computational Investigation of Shock-Shock Interactions at Mach 6. (Daytona Beach, FL 2013), TFAWS.
- 35 Fay, J. A. and Riddell, F. R. Theory of Stagnation Point Heat Transfer in Dissociated Air. *Journal of the Aeronautical Sciences*, 25, 2 (February 1958), 73-85, 121.